

To the Graduate Council:

I am submitting herewith a thesis written by Jason Bane entitled "The EMC Effect in A=3 Nuclei." I have examined the final paper copy of this thesis for form and content and recommend that it be accepted in partial fulfillment of the requirements for the degree of Doctor of Philosophy, with a major in Nuclear Physics.

---

Nadia Fomin, Major Professor

We have read this thesis  
and recommend its acceptance:

---

Jamie Coble

---

Kate Jones

---

Thomas Papenbrock

---

Soren Soreson

Accepted for the Council:

---

Carolyn R. Hodges

Vice Provost and Dean of the Graduate School

To the Graduate Council:

I am submitting herewith a thesis written by Jason Bane entitled “The EMC Effect in A=3 Nuclei.” I have examined the final electronic copy of this thesis for form and content and recommend that it be accepted in partial fulfillment of the requirements for the degree of Doctor of Philosophy, with a major in Nuclear Physics.

Nadia Fomin, Major Professor

We have read this thesis  
and recommend its acceptance:

Jamie Coble

---

Kate Jones

---

Thomas Papenbrock

---

Soren Soreson

---

Accepted for the Council:

Carolyn R. Hodges

---

Vice Provost and Dean of the Graduate School

(Original signatures are on file with official student records.)

# **The EMC Effect in A=3 Nuclei**

A Thesis Presented for  
The Doctor of Philosophy  
Degree

The University of Tennessee, Knoxville

Jason Bane

December 2018

© by Jason Bane, 2018

All Rights Reserved.

# Contents

<b>List of Tables</b>	<b>v</b>
<b>List of Figures</b>	<b>vi</b>
<b>1 Introduction</b>	<b>1</b>
1.1 Electron scattering . . . . .	2
1.1.1 Deep inelastic scattering . . . . .	5
1.2 EMC Effect . . . . .	8
1.3 MARATHON . . . . .	11
<b>2 Experimental Setup</b>	<b>12</b>
2.1 Thomas Jefferson Lab . . . . .	12
2.1.1 CEBAF . . . . .	12
2.1.2 Injector . . . . .	13
2.1.3 Accelerator . . . . .	14
2.2 Hall A Beam Line . . . . .	16
2.2.1 Beam Position Monitors . . . . .	16
2.2.2 Raster . . . . .	19
2.2.3 Beam Energy . . . . .	22
2.2.4 Beam Current Monitors . . . . .	23
2.3 Target . . . . .	25
2.4 High Resolution Spectrometers . . . . .	26

2.4.1	Vertical Drift Chambers	28
2.4.2	Scintillators	33
2.4.3	Cherenkov	34
2.4.4	Calorimeter	36
2.5	Trigger Setup	37
2.6	Kinematic Settings	37
<b>3</b>	<b>Data Analysis</b>	<b>39</b>
3.1	Efficiencies	39
3.1.1	Computer and electronic Lifetime	39
3.1.2	Particle Identification Efficiency	40
3.1.3		43
3.1.4		45
3.2	Background Subtraction	46
3.2.1	End Caps	46
3.2.2	Pair Produced Electrons	48
<b>4</b>	<b>Results</b>	<b>49</b>
<b>5</b>	<b>EMC Simulation</b>	<b>50</b>
5.1	Investigation	50
5.2	Transformation	51
5.3	Results	53
<b>6</b>	<b>Conclusion</b>	<b>56</b>
	<b>Bibliography</b>	<b>57</b>

# List of Tables

3.1 Livetime during the MARATHON experiment calculated using trigger 2. . . . .	40
--	----

# List of Figures

1.1	Simple Feynman diagram of an electron scattering from a proton [11].	3
1.2	Measurement of the proton structure function $F_2(x, Q^2)$ [2] . . . . .	7
1.3	Table of leptons, quarks and bosons with mass, charge and spin [26]. . . . .	8
1.4	Graph of the ratio of A/D structure functions vs $x$ for Carbon [16]. . . . .	9
1.5	EMC effect from EMC, SLAC, and BCDMS [27] . . . . .	10
1.6	Graph of the ratio of A/D structure functions vs $x$ for Carbon [16]. . . . .	11
2.1	Drawing of the Injector layout. . . . .	13
2.2	Schematic Layout of CEBAF. . . . .	15
2.3	A 3D drawing of Hall A. . . . .	16
2.4	A schematic layout of the beam line in Hall. [1] . . . . .	17
2.5	BPM design diagram, from JLab instrumentation group. Beam direction is from left to right [37]. . . . .	18
2.6	A schematic layout of a harp fork [37] . . . . .	19
2.7	The X and Y position for a Bulls eye scan for BPM calibration. . . . .	20
2.8	The X and Y current of the raster with a carbon hole. The size of the carbon hole is fit with a radial sigmoid[14]. . . . .	21
2.9	Hall A Current Monitor components [8]. . . . .	23
2.10	BCM calibration [28]. . . . .	24
2.11	BCM frequency for BCM calibration [28]. . . . .	25
2.12	Target Images . . . . .	26
2.13	A side view of a HRS [1]. . . . .	27

2.14 A view of both the left(top) and right(bottom) detector stacks inside the left and right HRS [1]. . . . .	28
2.15 A sketch of the two VDC planes in the HRSs with a particle traveling through the detector at 45°.[10]. . . . .	29
2.16 A possible track that causes signals in wires. The drift electrons will follow the arrow path. The dot/dashed lines correspond to the projected distance used to reconstruct the path of the incident particle. The transition point from parallel to radial field lines is represented by the ellipses. [10] . . . . .	30
2.17 The VDC efficiency for one plane of wires. . . . .	31
2.18 Histograms of VDC signals before(left) and after(right) calibration of t0[19]. . . . .	32
2.19 Histogram of $\beta$ before and after time walk correction. . . . .	33
2.20 Top down depiction inside the GC [4]. . . . .	34
2.21 The raw signal captured from a single cherenkov PMT, PMT[1], with a fit to the pedestal peak and a line draw to demonstrate its ADC channel number. . . . .	35
2.22 Left: The sum of all ADC channels from the LHRs calorimeters. Right: The total energy deposited into the LHRs calorimeter scaled by the momentum setting. Electron cuts have been applied. . . . .	37
2.23 Scematic drawing of the trigger logic and timing for the MARATHON experiment [15]. . . . .	38
3.1 Two dimensional plot of the cherenkov sum versus Total Energy deposited, including electron sampling in teal and non-electron sampling in red. . . . .	41

3.2	Electrons and other back ground particles identified via cuts in the total calorimeter and the gas cherenkov shown in the individual layers of the calorimeters and the cherenkov. Sampling cuts for Electrons in teal and Non-Electrons in red. . . . .	42
3.3	The PID efficiency for the cherenkov and both layers of the calorimeter,including the overall total PID efficiency for each of the gas targets at all of the kinematics. . . . .	43
3.4	Trigger efficiency of trigger 2 for different targets at all kinematics calculated via sampling from trigger 1. . . . .	44
3.5	Tracking efficiency of the VDCs for different targets at all kinematics.	45
3.6	Comparison of the scattering vertex along the z axis for the empty target(EM) and the gas targets at kin. 4. . . . .	47
3.7	The ratio of positron events to electrons for tritium [33]. . . . .	48
5.1	Example of the electron beam(red) with a energy of 2.5 GeV and the proton(blue) with angle of $45^\circ$ in respect to the electron and with a momentum of 0.5 GeV/c. . . . .	51
5.2	Vector representations of the momentum for the incoming electron(red) and target proton(blue) with units of GeV for each phase of their transformations before scattering. . . . .	52
5.3	Vector representations of the momentum for the incoming electron(red) and target proton(blue) with units of GeV for each phase of their transformations after scattering). . . . .	54
5.4	Simulation results for fixed momentum protons. Three runs with unique proton momentum. . . . .	55

# Chapter 1

## Introduction

Understanding the world around us is the goal of every scientist, from the chemist that experiments with the formation of atoms to the geologist exploring the process of rock formations. Nuclear physicists focus on studying the fundamental constituents of matter, the building blocks of nature. Physicist use scattering experiments at accelerator facilities, like CERN in Switzerland, DESY in Germany, BATES in Massachusetts, JLAB in Virginia, and many others, to study the protons and neutrons and their constituents that make up a nucleus. These experiments allow physicists to observe the internal structure of the nucleus and to investigate the interactions between the quarks and gluons. Many of the experiments are design to confirm a existing results while also expanding on unique ideas.

In the last century, there have been numerous breakthroughs in the fields of nuclear and particle physics. Rutherford discovered the proton by bombarding light nuclei with alpha particles to produce



This reaction allowed Rutherford to conclude that the Hydrogen nucleus was a constituent of an atomic nuclei [30]. In the late 1950s, experimental results published

by W. McAllister and R. Hofstadter exposed some of the eternal structure of the proton [11, 24]. The European Muon Collaboration(EMC) produced results in the early 1980s showing a differences between the internal structure of the deuterium nucleus and Iron [32, 16]. The data received from scattering experiments using alpha particles contain information about the target, the beam, and the interaction between the two. Deciphering and analyzing this data can be convoluted because the cross-section contains information about the internal structure of the target and the beam along with the interaction and forces between the two [30].

This thesis will discuss using deep inelastic scattering to study the internal structure of two light nuclei as a part of the E12-010-103 experiment. The discussion will include the motivations, approach, and the outcome from one analysis technique.

## 1.1 Electron scattering

In order to remove some of the complexity in scattering experiments, one may employ highly relativistic electrons. Electrons being point-like particles without any internal structure allow the elimination of some of the analysis difficulties with using alpha particles in scattering experiments due to their complex internal structure. Electrons and the target nucleus, nucleon, or quarks interact via the exchange of a virtual photon. Using quantum electrodynamics (QED), these interactions can accurately be described by the well known electromagnetic interaction. Higher order terms of this process contribute very little due to the coupling constant  $\alpha \approx 1/137$ , being much smaller than one.

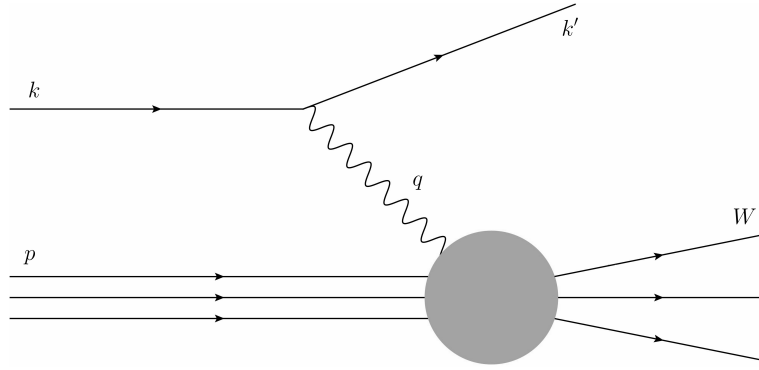
Figure 1.1 represents an electron scattering from a proton. The incoming or incident electron's four-momentum is described as  $k = (E, \vec{k})$  and the scattering electron's four-momentum is represented by  $k' = (E', \vec{k}')$ . The exchange of the virtual photon in this

electromagnetic interaction is defined by the four-momentum transfer  $q$ :

$$Q^2 \equiv -q^2 = 4EE' \sin^2(\theta/2). \quad (1.2)$$

In equation 1.2,  $E$  and  $E'$  are the electron energy before and after the scattering interaction. Theta is the angle that describes the deflection of  $E'$  from the electron's original path.

**Figure 1.1:** Simple Feynman diagram of an electron scattering from a proton [11].



Along with  $Q^2$ , the variables  $\nu$ ,  $W$ , and  $x_B$  are used to narrate the evolution of the electron scattering process.  $\nu$ , defined as  $p \cdot q/M$ . In the rest frame of the target,  $\nu$  can be described by:

$$\nu = E - E'. \quad (1.3)$$

Simply,  $\nu$  is the magnitude of energy loss by the electron during the scattering interaction. The invariant mass of the system,  $W$ , defines the hadronic state produced by the scattering event.

$$W^2 \equiv (q + p)^2 = M^2 + 2M\nu - Q^2. \quad (1.4)$$

A scattering event with the invariant mass equal to the square of the mass of the nucleon, ( $M^2$ ), falls in the regime of elastic scattering.  $W$  above  $M^2$  will transform

the scattering interaction from an elastic scattering to inelastic scattering due to the excited state of the scattered byproduct.

The intrinsic likelihood of an event with a certain  $Q^2$ ,  $\nu$ , and  $W$  is defined by the scattering cross section. An electron scattering off of a target with a charge of  $Z * e$  can be described by the Rutherford cross-section. Povh et. al. details the Rutherford cross section as:

$$\left( \frac{d\sigma}{d\Omega} \right)_{Rutherford} = \frac{(zZe^2)^2}{(4\pi\epsilon_0)^2 * (eE_{kin})^2 \sin^4(\theta/2)}. \quad (1.5)$$

In the early 1920s, German physicists Stern and Gerlach performed an experiment that confirmed the presence of electron angular momentum. Later a discovery of electron spin was made by Uhlenbeck and Goudsmit. The Rutherford cross-section neglects the spin of an electron and its target. The Mott cross-section is the evolved version of the Rutherford cross-section. It has been modified to include the intrinsic spin of the target and electron. The Mott cross-section is: [18, 30]

$$\left( \frac{d\sigma}{d\Omega} \right)_{Mott} = \frac{4Z^2\alpha^2(\hbar c)^2 E'^2}{|\mathbf{q}c|^4} \cos^2(\theta/2). \quad (1.6)$$

There is an agreement between the measured cross section and the theoretical Mott cross-section when in the limit of  $|\mathbf{q}| \rightarrow 0$  for scattering events of electrons off of a target nuclei. As  $|\mathbf{q}|$  climbs furtherer from zero, the experimentally measured cross sections systematically decreases [30]. Increasing the  $|\mathbf{q}|$  of an interaction reduces the size of the wavelength of the virtual photon that mediates the electromagnetic interaction between the electron and target nuclei and increases the resolution of the probe. The wavelength of this virtual photon is inversely proportional to  $|\mathbf{q}|$ , and can be described by the following:  $\lambda = \frac{\hbar}{|\mathbf{q}|}$  [30]. Increasing the amount of momentum transferred in an electromagnetic reaction allows one to study deeper into the nucleus.

Studying the internal structure of a nucleus with the electromagnetic interaction requires increasing the momentum transferred. Pushing  $|\mathbf{q}|$  to be comparable with the mass of a nucleon adds more complexity to the details of the scattering interaction. At the appropriate levels of  $|\mathbf{q}|$  to study the nucleons in the nucleus, the Mott cross-section equation requires modifications to include additional factors that incorporate information about the target. The Rosenbluth formula is based on the Mott cross section and embraces target recoil, magnetic moment, and charge and current distributions. Povh writes the Rosenbluth formula as:

$$\left(\frac{d\sigma}{d\Omega}\right) = \left(\frac{d\sigma}{d\Omega}\right)_{Mott} * \left[ \frac{G_E^2(Q^2) + \tau G_M^2(Q^2)}{1 + \tau} + 2\tau G_M^2(Q^2) \tan^2 \frac{\theta}{2} \right]. \quad (1.7)$$

Equation 1.7 contains  $G_E^2(Q^2)$  and  $G_M^2(Q^2)$ , the electric and magnetic form factors.  $\tau$  is used in the Rosenbluth formalism to account for the magnetic moment of a nucleon and is defined as:  $\tau = \frac{Q^2}{4M^2c^2}$  [30]. In the general case of electron scattering off of a free proton or neutron elastically, the scattered energy of the electron will be a function of the incident electron's energy and the scattered angle of the electron, shown in the following equation.

$$E' = \frac{E}{1 + \frac{E}{Mc^2}(1 - \cos\theta)} \quad (1.8)$$

### 1.1.1 Deep inelastic scattering

The first generation of electron scattering experiments achieving a significantly large  $|\mathbf{q}|$  used a linear accelerator with a 25 GeV maximum beam energy, and following generations increased the total interaction energy to substantially higher thresholds. At these high incident beam energies, individual resonances cannot be separated in the invariant mass spectrum above 2.5 GeV. Observations made into this convoluted invariant mass spectrum has shown that many strongly interacting particles are produced, known as hadrons. Scattering interactions that generate these hadrons are considered to be inelastic.

Inelastic scattering events contain the possibility of conceiving additional resultants causing an increase in the complexity of a scattering interaction. In order to create an inelastic event, the wavelength of the virtual photon has to be comparable to the radius of the struck nucleon. Increasing the amount of transferred momentum so that  $Q^2 R^2 \gtrsim 1$ , will increase the resolution of the probe to a level that allows for the interaction to be with the charge constituents within the nucleon. When the scattering event probes the fundamental elements of a nucleon, the scattering process is titled deep inelastic scattering(DIS). Due to the increase in complexity, an additional degree of freedom has to be introduced into the scattering cross section formalism. Modifying the Rosenbluth formula to include the inelastic scattering structure functions  $F_1(Q^2, \nu)$  and  $F_2(Q^2, \nu)$  evolves the Rosenbluth formula to contain the needed complexity of an inelastic event. These modifications are shown in equation 1.9. The  $F_1$  and  $F_2$  structure functions provide the details for describing the internal composition of the nucleon [30].

$$\frac{d^2\sigma}{d\Omega dE'} = \left( \frac{d\sigma}{d\Omega} \right)_{Mott} \left[ \frac{F_2(Q^2, \nu)}{\nu} + \frac{2F_1(Q^2, \nu)}{M} \tan^2 \frac{\theta}{2} \right]. \quad (1.9)$$

In the case of DIS off of a proton, the electron probe is used to explore the exclusive internal structure of the proton. In 1969, Feynman assumed the internal make up of the proton was that of point-like partons [6, 21], the basis of the parton model. As part of this model, the impulse approximation makes an assumption that the duration of the interaction between the mediating photon and parton is relatively short, allowing for the interaction between individual partons to be neglected. Thus in a DIS interaction, the partons can be described as free, with minimal internal interactions. Under this understanding, a electron-nucleon DIS interaction would characterize the properties and motions of the partons that make up the struck nucleon[21]. The characteristics, the motions and properties, of the partons are formalized into a parton distribution function  $f_i(x_B)$ . The Bjorken scaling variable,  $x_B, x$ , is a dimensionless quantity that measures the in-elasticity of a scattering process

and is defined as:  $x := \frac{Q^2}{2M\nu}$ . The parton distribution functions can be used to relate the  $F_1$  and  $F_2$  structure functions used in equation 1.9 [30].

$$F_2(x) = x \sum_i e_i^2 f_i(x) \quad (1.10)$$

$$F_1(x) = \frac{1}{2x} F_2(x)$$

$$F_2(x) = x \cdot \sum_f z_f^2 (q_f(x) + \bar{q}_f(x)) \quad (1.11)$$

Measurements from the Standford Linear Accelerator(SLAC) In the Bjorken limit,  $v \rightarrow \infty$  and  $Q^2 \rightarrow \infty$ , the deep inelastic structure functions can be described as functions of only  $x$ .

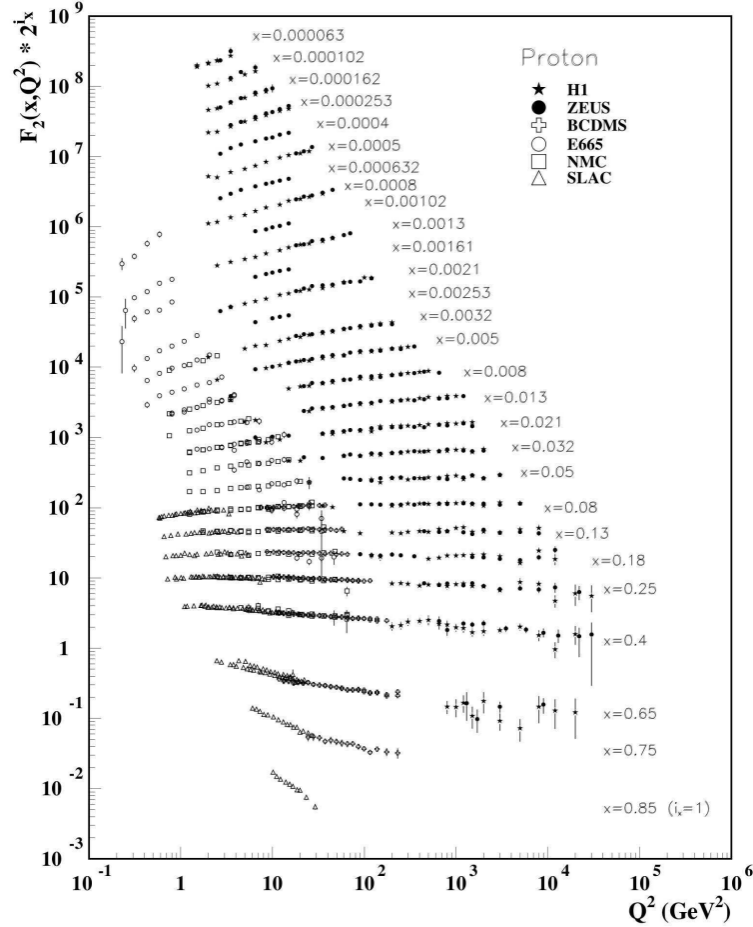


**Figure 1.2:** Measurement of the proton structure function  $F_2(x, Q^2)$  [2] .

Three Generations of Matter (Fermions)				
	I	II	III	
mass →	2.4 MeV	1.27 GeV	171.2 GeV	
charge →	$\frac{2}{3}$	$\frac{2}{3}$	$\frac{2}{3}$	
spin →	$\frac{1}{2}$	$\frac{1}{2}$	$\frac{1}{2}$	
name →	u up	c charm	t top	
			$\gamma$ photon	
Quarks	d $\frac{-1}{3}$ down	s $\frac{-1}{3}$ strange	b $\frac{-1}{3}$ bottom	g gluon
Leptons	$<2.2$ eV 0 $\frac{1}{2}$ e electron neutrino	$<0.17$ MeV 0 $\frac{1}{2}$ $\nu_\mu$ muon neutrino	$<15.5$ MeV 0 $\frac{1}{2}\nu_\tau$ tau neutrino	91.2 GeV 0 $Z^0$ weak force
	e $-1$ $\frac{1}{2}$ e electron	$105.7$ MeV $-1$ $\frac{1}{2}\mu$ muon	$1.777$ GeV $-1$ $\frac{1}{2}\tau$ Tau	$80.4$ GeV $\pm 1$ $\frac{1}{2}W^\pm$ weak force
Gauge Bosons				

**Figure 1.3:** Table of leptons, quarks and bosons with mass, charge and spin [26].

[34] [21] [36] [5]

## 1.2 EMC Effect

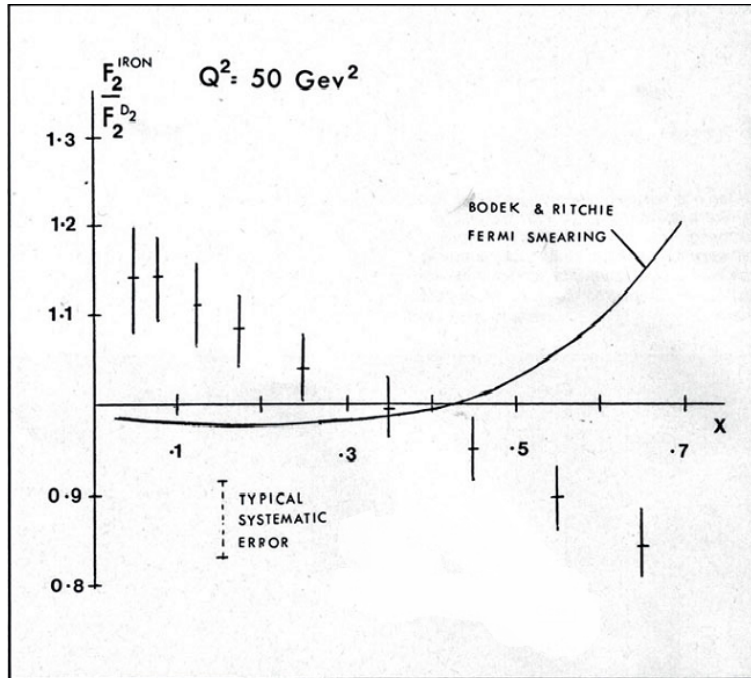
The European Muon Collaboration (EMC) performed a deep inelastic measurement with 120-280 GeV muons on iron and deuteron targets [23]. The EMC extracted A/D structure function ratios versus the Bjorken scaling variable,  $x$ . The relationship originally expected by the EMC contained the sum of the structure functions of each nucleon in a nucleus. Each nucleus has a certain number of neutrons ( $N$ ) and a amount of protons ( $Z$ ). The expected structure function for a nucleus could be written as:

$$F_A = NF_2^N + ZF_2^P. \quad (1.12)$$

The EMC compared the extracted structure functions from iron and deuterium. Their results are shown in Figure 1.4. The  $\frac{A}{D}$  structure function ratio showed an unexpected downward slope. This phenomenon was titled the EMC effect.

This finding demonstrated to the EMC that their understanding of the nucleus was incorrect. A nucleon's structure function and thereby, the constituent quark distributions may be altered by the nucleus.

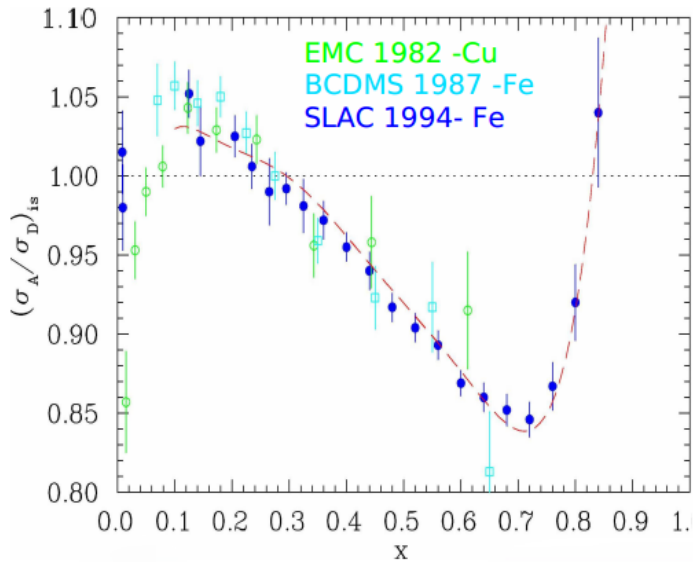
**Figure 1.4:** Graph of the ratio of A/D structure functions vs  $x$  for Carbon [16].



Ever since the European Muon Collaboration discovered the depletion of quarks at high  $x$  for  $A > 2$  nuclei, physicists have tried to discover its cause. Scientists at SLAC extracted structure function ratios for many nuclei including;  ${}^4\text{He}$ ,  ${}^9\text{Be}$ ,  ${}^{12}\text{C}$ ,  ${}^{27}\text{Al}$ ,  ${}^{40}\text{Ca}$ ,  ${}^{56}\text{Fe}$ ,  ${}^{108}\text{Ag}$ , and  ${}^{197}\text{Au}$ . There were slightly different results for each nucleus. The magnitude of the EMC effect, taken to be the A/D ratio at  $x = 0.6$ , was found to be different for the various nuclei, and roughly scaled with the size or density of the nuclei. The NMC (New Muon collaboration), another group at CERN, gathered precise data in order to construct the inclusive cross section of deuterium and protons. BCDMS collaboration extracted data for N and Fe structure function ratios. Figure 1.5 shows some of the data from SLAC and BCDMS on the EMC effect for Iron and Cu. Figure 1.6 shows this result from a recent JLab EMC measurement, most

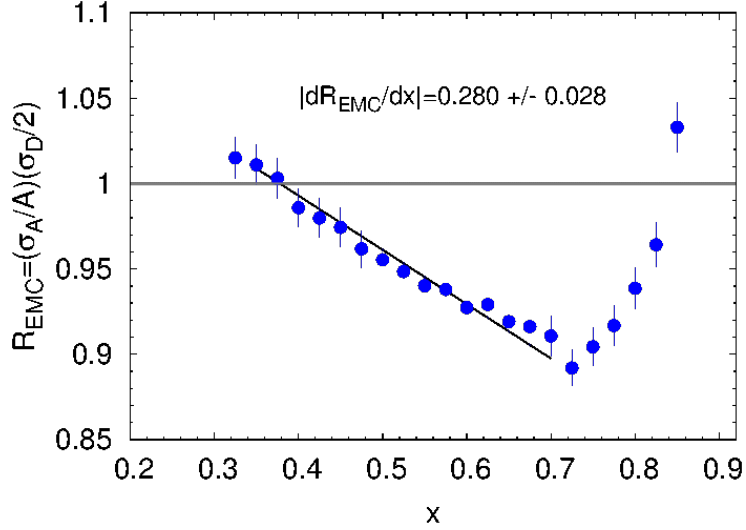
precise to date. Many models over the years have been able to reproduce the shape of the A/D ratios. These models can contain traditional nuclear physics effects like momentum distribution or pion-charge contributions. Some models also describe the EMC effect through quark momentum distribution or modification of the internal structure [27, 9, 3, 12, 13]. However, no single model has provided a complete picture of the possible underlying physics. Precise data from Jlab's E03-103 experiment has revitalized this research. This experiment focused on precision measurements in light nuclei and added  ${}^3\text{He}$  as a target nucleus. Instead of taking the A/D ratio at a certain  $x$ -value to be the magnitude of the EMC effect, this analysis looked at the slope instead. This eliminated sensitivity to normalization uncertainties.

**Figure 1.5:** EMC effect from EMC, SLAC, and BCDMS [27]



In Figure ,  ${}^9\text{Be}$  was found not to follow the previously observed scaling with nuclear density. This result from Jefferson Lab determined that the previous idea of a dependence on A or nuclear density in the EMC effect to be incorrect [32]. This result spawned a drive to determine another explanation for the EMC effect and understand what clue the  ${}^9\text{Be}$  outlier was providing. The structure of this nucleus

**Figure 1.6:** Graph of the ratio of A/D structure functions vs  $x$  for Carbon [16].



is made up of two high-density alpha particles and a single neutron [7]. The regions of higher density that are contained in a comparatively large volume may be able to explain why  ${}^9\text{Be}$  does not follow the expected trend. This suggests that the EMC effect could be a function of local nuclear density [32].

### 1.3 MARATHON

Experiment E12-010-102, MARATHON (MeAsurement of the  $F2^n/F_2^p, d/u$  RAtios and A=3 EMC Effect in Deep Inelastic Electron Scattering Off the Tritium and Helium MirrOr Nuclei), will use deep inelastic scattering off of the mirror nuclei  ${}^3\text{H}$  and  ${}^3\text{He}$  to measure the EMC effect for both  ${}^3\text{H}$  and  ${}^3\text{He}$ , to determine the ratio of the neutron to proton inelastic structure functions, and to find the ratio of the down to up quark distributions in the nucleon.

# **Chapter 2**

## **Experimental Setup**

### **2.1 Thomas Jefferson Lab**

Thomas Jefferson Lab (Jlab) in Newport News, Virginia hosted the MARATHON experiment in the Fall of 2017 and Spring of 2018. Jlab uses support from the U.S. Department of Energy(DOE) and the state of Virgina to complete the lab's mission of delivering productive research by exploring the atomic nucleus and its fundamental constituents, including precise tests of their interactions. Along with applying an advanced particle accelerator, particle detectors and other technologies to develop new basic research capabilities and to address the challenges of a modern society.

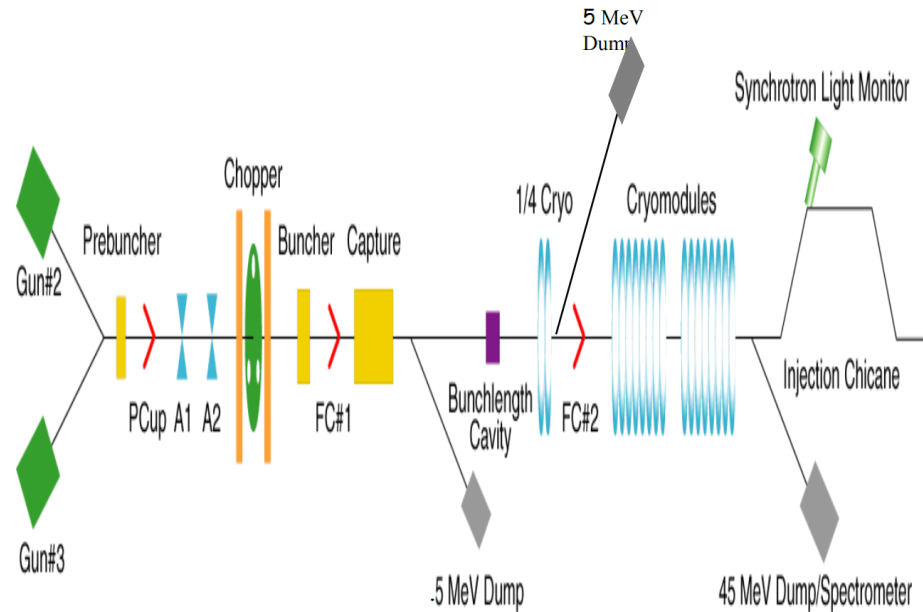
#### **2.1.1 CEBAF**

The Continuous Electron Beam Accelerator Facility (CEBAF) was recently upgraded to a 12 GeV accelerator, upgrading it to be able to supply a 11 GeV beam of continuous electrons of up to  $200 \mu\text{A}$  of current to three experimental halls (A,B,C) and 12 GeV to the recently constructed hall D.

## 2.1.2 Injector

CEBAF uses a micro-pulsed structure from the photo-electron gun to produce electrons in an efficient manner. This micro-pulsed structure is used to prolong the lifetime of the photocathode. The delivery of unique current and energy to all four halls requires the micro-pulses to have a 250 MHz or 500MHz structure and four individually tuned lasers. Frequencies of 250 MHz and 500MHz are chosen because these are sub-harmonics of the fundamental accelerator operating frequency of 1500 MHz.

**Figure 2.1:** Drawing of the Injector layout.



Electrons are produced when laser light shines on a gallium arsenide photo cathode. A laser pulse excites electrons from the photo cathode via the photoelectric effect. These excited electrons form from the gallium arsenide wafer when the electrons are excited out of the valence band into the conduction band. Gallium arsenide was chosen because the energy level of the conduction band for this photo cathode sits above the energy of an electron vacuum. Electrons in the conduction band escape

from the material and are accelerated away from the wafer due to high negative potential on the photo cathode wafer [26].

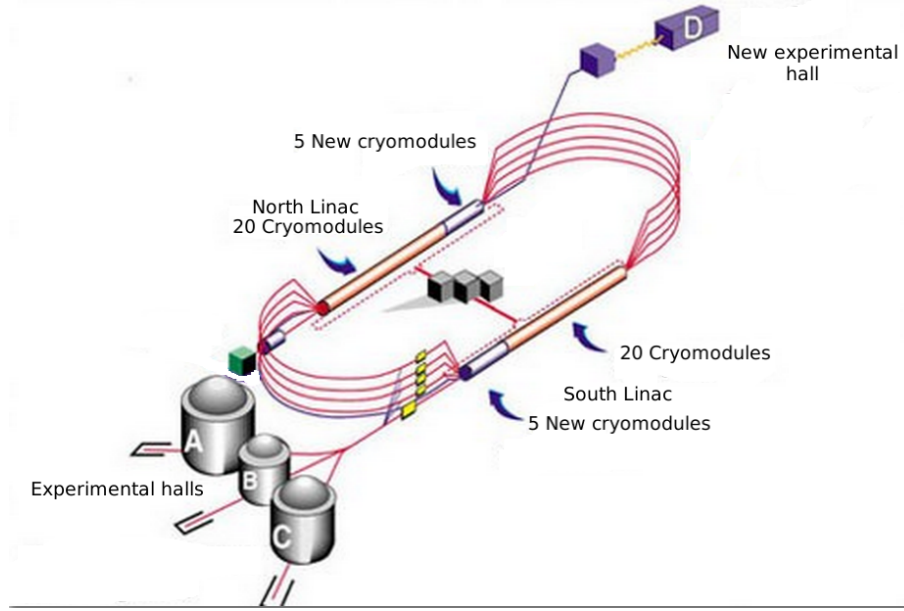
These electrons are accelerated into the injector beam line via the electron gun. Tunning the amount of electrons in a bunch happens at the chopper. Slits in the chopper allow for greater regulation of the currents sent to the four experimental halls. Testing and calibration of the four beams are done throughout the injector beam lines via the Faraday cups located at different spots in the beam line. The polarized gun can supply electrons with up to 80% polarization and the polarization direction can be controlled by a wien filter. To ensure the level of polarization, a 5 MeV Mott polarimeter may be used to measure the level of polarization[1]. The injector accelerates the electrons up to 123 MeV before allowing them into the north LINAC [22, 29, 20].

### 2.1.3 Accelerator

The electrons are conveyed through two LINACs and two bending arcs per complete pass of the accelerator. The two LINACs are approximately a quarter mile long and are thirty feet below the surface. The beam lines are kept under vacuum between  $E^{-6}$  and  $E^{-11}$  torr to provided an efficient medium for transfer. Electrons traveling to Halls A, B, and C complete a maximum of four and a half revolutions around the accelerator. These particles receive approximately 2.2 GeV in energy for each cycle through the accelerator.

The radio frequency (RF) cavities in each LINAC use an oscillating electromagnetic field to supply a force to accelerate the passing electrons. These Niobium RF cavities are cooled to 2 K in order to create conditions that allow the cavities to be superconducting [1]. The superconduction RF(SRF) cavities provided a negatively charge field behind the electrons and positively charged field in front to accelerate the electrons through a set of cavities inside a cryomodule. A central helium liquefier

**Figure 2.2:** Schematic Layout of CEBAF.

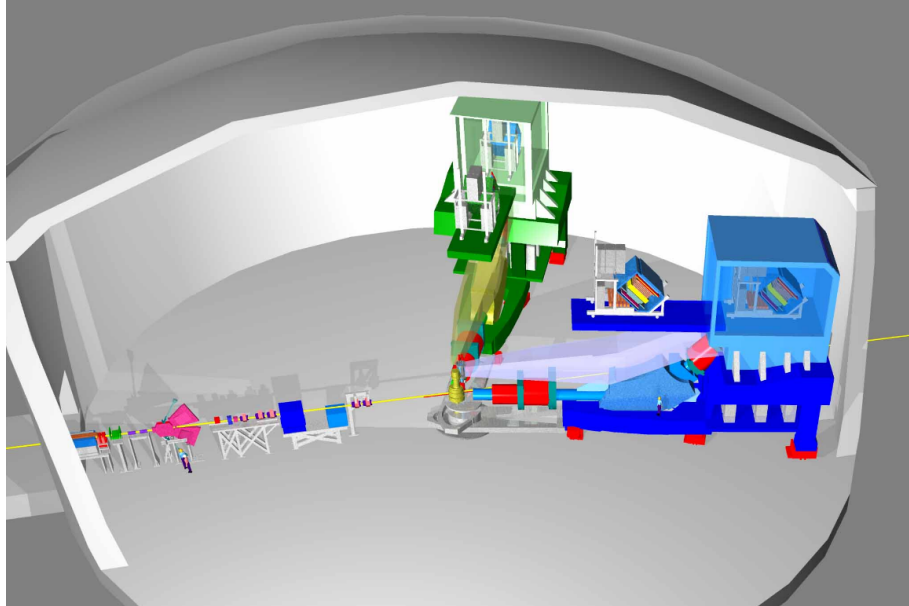


circulates up to 17000 gallons of chilled liquid helium to control the temperature of the cryomodules. A dedicated 5 kW klystron provides a 1500 Mhz RF driving signal for each cryomodules.

The electron beam exiting the north LINAC enters the east arc. The east and west arcs contain large dipole and quadrupole magnets to steer and focus the beam as the beam is accelerated back to the other LINAC. After electrons exit the south LINAC, they either continue on around the accelerator for another pass to increase in energy, or a RF separator projects the electron beam into the proper experiment hall [22]. Energy loss, beam position, and beam charge monitors lie throughout the beam line, and are used to insure the quality of beam delivered to the halls.

## 2.2 Hall A Beam Line

**Figure 2.3:** A 3D drawing of Hall A.



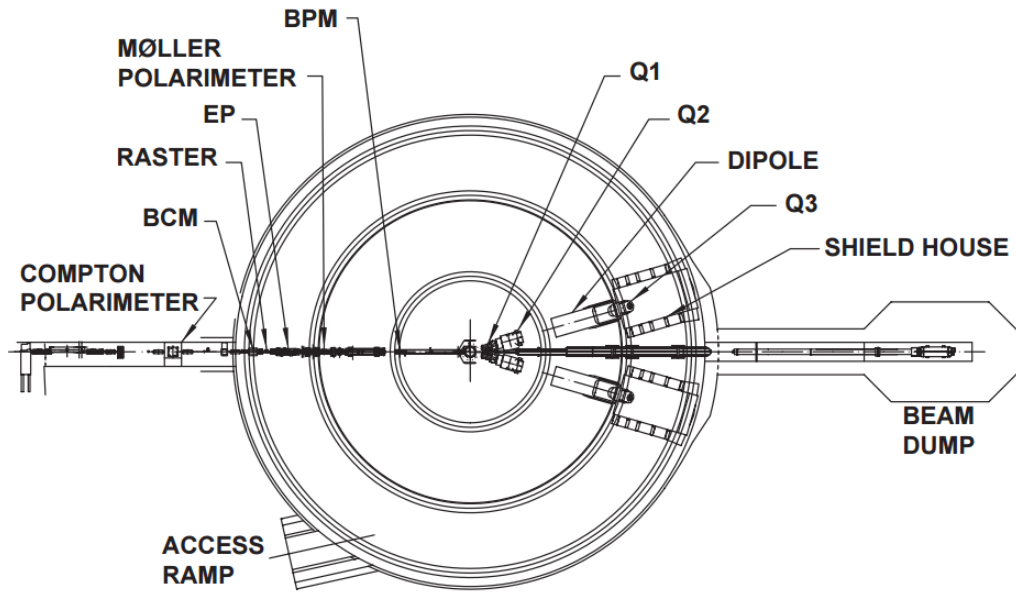
The experimental Hall A and the scientific equipment used were designed for detailed investigations of the internal structure of nuclei. Two high resolution spectrometers in Hall A use the inclusive ( $e,e'$ ) and exclusive ( $e,e' p$ ) reactions to gain a greater understanding of the structure of the nucleus. Completing detailed studies with high resolution and extreme accuracy requires knowing the beam position, size, energy, and current when the beam strikes the target. The instrumentation used in the precise measurement of these quantities in Hall A are shown in figure 2.4 [1]. The information provided by these detectors originate through small changes in current and voltage sent through the electronics. These signals are transformed into useful information through calibrations.

### 2.2.1 Beam Position Monitors

A pair of Beam Position Monitors(BPM)s are used to measure the relative beam position without affecting the beam. The two Hall A BPMs are located at 7.524 m

and 1.286 m away from the target. Using the standard difference-over-sum technique, the relative beam position is determined with an accuracy of 100  $\mu\text{m}$  with a beam current of at least 1  $\mu\text{A}$  [1]. The BPMs' positional data is recorded in two ways. Every second of beam time, the beam position average over 0.3 seconds is logged into the Experimental Physics and Industrial Control System (EPICS) database. The BPMs also transmit data event-by-event to the CEBAF online Data Acquisition system(CODA).

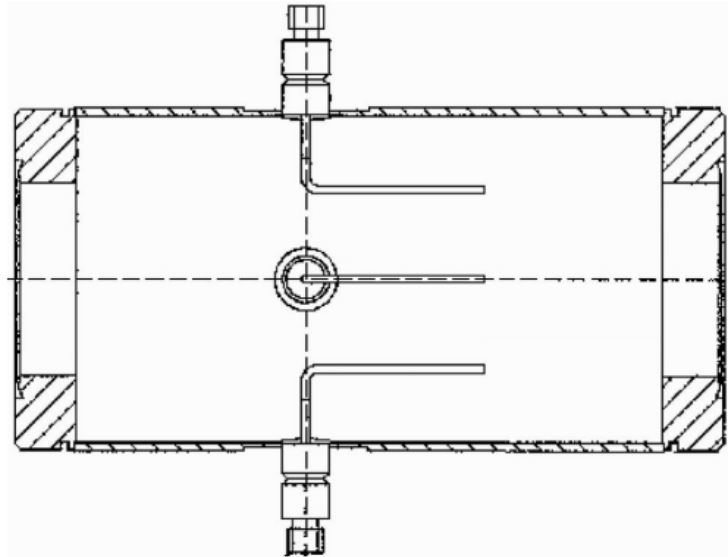
**Figure 2.4:** A schematic layout of the beam line in Hall. [1]



The main beam line components of the BPMs consist of four open-ended antennas. Figure 2.5 shows a BPM chamber and figure ?? shows the layout of the four antennas as you look down the beam line. In this chamber, the design of three of the four antennas can be seen. The antennas are titled  $u_+$ ,  $u_-$  and  $v_+$ ,  $v_-$ . The antennas receive an induced signal as electrons pass to determine the beam position in the  $u$  and  $v$  directions. The BPMs send a DC offset to the DAQ. This DC offset is turned into a positional measurement via looking at both signals in one direction. The position in the frame of the  $u$  and  $v$  antennas are calculated by taking the

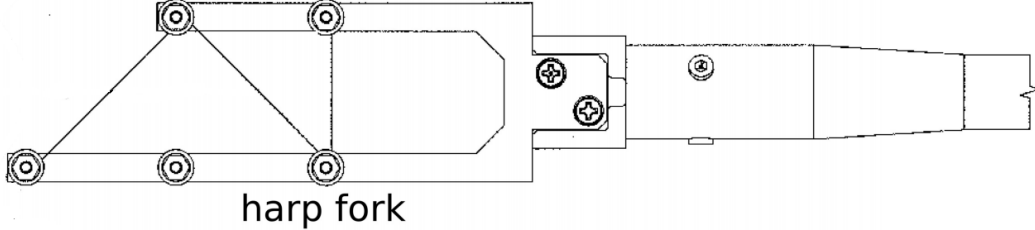
difference over the sum of the two wires in the u and v directions. The accuracy of the BPMs requires an absolute measurement of the electron beam's position to calibrate the BPMs[31, 37].

**Figure 2.5:** BPM design diagram, from JLab instrumentation group. Beam direction is from left to right [37].



Two harps were used to provide the absolute measurement required for the calibrations. Each harp is located immediately after the BPM on the beam line. The harp forks are aligned perpendicular to the beam line to allow the harps to be moved in and out of the beam line. A wire that transverse between the fork tines at three different angles in respect to the harp is used to determine the horizontal and vertical position of the beam. The two sloped sections of the wire are angled at  $45^\circ$  relative to the harp frame. As the harp fork is moved into the beam, the wires receive a signal as the beam interacts with the wires. The two sloped wires are used together to determine the vertical position of the beam. The vertical wire is used to determine the horizontal position of the beam [31, 37]. The harps are not used during production phases due their intrusive nature caused by the interaction of the beam with the harp wire.

**Figure 2.6:** A schematic layout of a harp fork [37]



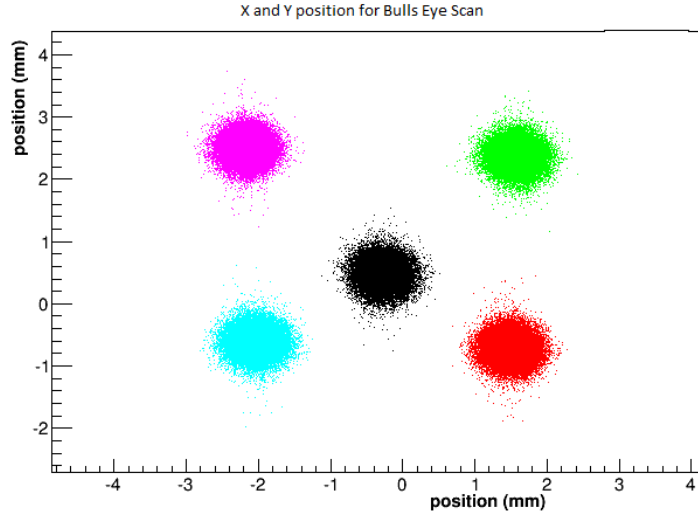
The location of the wires on the harp frame and the position of the harp fork were used to calculate the absolute beam position. Figure 2.7 shows an example of five positions used to calculate the BPM calibration coefficients. This method of using beam positions at the nominal center and surrounding the center is called a bull's eye scan. The harp scan results are substituted into equation 2.1 for the X and Y positions. Using all five points and an  $R^2$  regression technique, the coefficients can be determined with great accuracy. These highly accurate BPMs were crucial in reducing systematic error in the final results obtained from this experiment.

$$\begin{pmatrix} X_{position} \\ Y_{position} \end{pmatrix} = \begin{pmatrix} C(0,0) & C(0,1) \\ C(0,0) & C(0,1) \end{pmatrix} * \begin{pmatrix} X_{BPM} \\ Y_{BPM} \end{pmatrix} + \begin{pmatrix} X_{offset} \\ Y_{offset} \end{pmatrix} \quad (2.1)$$

### 2.2.2 Raster

Damage to a target system from intense beam can cause extreme fluctuations in the target's temperature and density. A raster was used to counteract the damage caused by a focused beam. The raster used two magnetic fields produced by two dipoles to spread the electron beam out. This produces a large rectangle interaction area on the front face of the target container. A triangle wave of 25 kHz was used to control the coils of the dipole magnets. The raster systems are located  $\approx 17$  meters before the target chamber (upstream of the target[37]). The rasters position can be seen in figure 2.3. Safety constraints administrated by the target group at JLAB

**Figure 2.7:** The X and Y position for a Bulls eye scan for BPM calibration.



limited the minimum size of the raster spot for the MARATHON experiment to two millimeters by two millimeters. This limit was installed has a safety concern for the tritium target.

The Hall A raster system consists of four dipoles. Two dipoles produce magnetic fields in the horizontal direction of the lab frame and two in the vertical. The upstream raster and downstream rasters include one vertical and one horizontal dipole. The relative change in position of the incoming electrons are controlled by the current supplied to the dipoles. This current that drives the dipoles is recorded by an ADC. In order to obtain the change in beam position due to the rasters, a calibration between the raster current and measured beam position were obtained.

The raster calibration is done by creating a line that maps the raster current measured by ADC bins to a position. This calibration process is done to extract positions at the locations of both BPMs and the target center along the beam line. The calibration of the linear mapping of raster current to beam position took two processes. The first process was to determine the size of the rastered beam spread. In

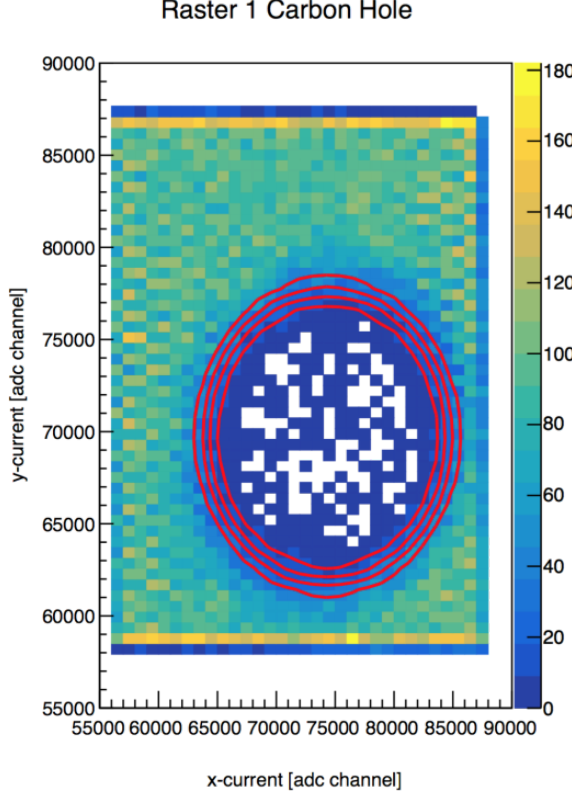


**Figure 2.8:** The X and Y current of the raster with a carbon hole. The size of the carbon hole is fit with a radial sigmoid[14].

order to accurately determine the width and height of the beam spread due to the raster, a carbon foil with a hole of a diameter of 2mm was used. A radial sigmoid was used to fit the hole. The fit of the carbon hole gives the width of the raster, the slope of the linear mapping term. In figure 2.8, the raster current in x and y directions are fitted using this radial sigmoid. Once the slope of the linear calibration is determined, the offsets can be found. This is discovered by using the calibrated BPM mean positions for a phase of rastered beam. The mean positions for both BPMA and BPMB are used to produce a track from the BPMs to the target. This projection provides a mean location of the beam at the target. Using equation 2.2, the offsets also known as the intercepts can be solved for using the slope ( $m_x, m_y$ ), the

raster mean current value ( $R_x, R_y$ ), and the mean BPM position( $x, y$ ). [14]

$$\begin{pmatrix} x \\ y \end{pmatrix} = \begin{pmatrix} R_x \\ R_y \end{pmatrix} * \begin{pmatrix} m_x & 0 \\ 0 & m_y \end{pmatrix} + \begin{pmatrix} O_x \\ O_y \end{pmatrix} \quad (2.2)$$

### 2.2.3 Beam Energy

The electron beam energy is located in many of the equations used in an electron scattering experiment. This can cause a noticeable increase in systematic error if the beam energy measurement is not made precisely. At JLAB for the MARATHON experiment, the beam energy was measured in two ways. In Hall A, the beam energy was measured by using the (e,e/p) method. On the beam line, 17 meters upstream from the target an ep scattering chamber is located. The beam was directed into the target containing a rotating 10-30  $\mu\text{m}$  thick tape of  $\text{CH}_2$ . The scattering angle of the electron and the recoil angle of the proton are used to determine the beam energy using equation 2.3. Where  $M_p$  is the mass of the proton and  $\theta_p, \theta_e$  are the scattered angle of the proton, electron respectively.

$$E = M_p \frac{\cos\theta_e + \frac{\sin\theta_e}{\tan\theta_p} - 1}{1 - \cos\theta_e} \quad (2.3)$$

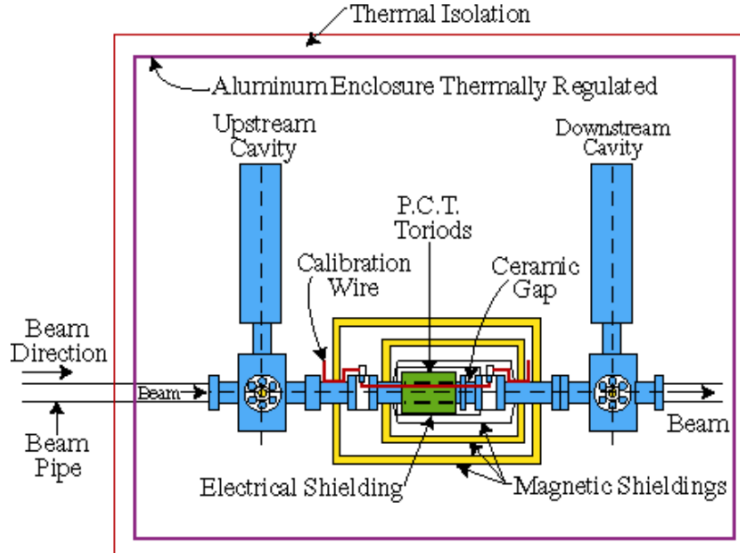
The beam energy was also measured using the ark measurement method [11]. This method uses changes in beam position and precise measurements of the magnetic fields around the beam line to determine the energy of the electron beam. The angle at which the electrons are bent through is related to the momentum of the electrons,

$$p = k \frac{\int \vec{B} \cdot d\vec{l}}{\theta}. \quad (2.4)$$

In equation 2.4,  $p$  is the momentum of the electrons,  $\theta$  is the bend angle, and  $\vec{B}$  is the magnetic field the electron experiences. Then using the momentum of the electron, the energy of the beam can be extracted. The error on the beam energy measurement

is  $\delta E/E \approx 2 * 10^{-4}$  [35, 11]. The MARATHON experiment used both methods to accurately determine the electron beam energy.

**Figure 2.9:** Hall A Current Monitor components [8].



## 2.2.4 Beam Current Monitors

The main process of measuring the scattering yield for a calculation of a cross section looks at finding the ratio of the number of electrons scattered to the number of electrons sent. In order to accurately determine the number of electrons sent to scatter with our target system, Hall A use a set non-invasive beam current monitors(BCMs). The Hall A BCMs have an absolute accuracy of 0.2 percent as long as the current is between 1 and 180  $\mu\text{A}$ . The BCMs used in Hall A consist of three main components: a Parametric Current Transformer (PCT) and two pill box cavities. Figure 2.9 shows the components in the Hall A BCM. The BCM produces an RF signal that is proportional to the beam current. A 10 kHz down converter, RMS-to-DC converter, voltage-to-Frequency converter, and a scaler are used to inject the current signal into the Hall A DAQ. Proportionality constants are determined in the calibration process to correctly integrate the charge for a given amount of beam current[8]. The process of calibrating the BCM converts the frequency received from the BCMs to

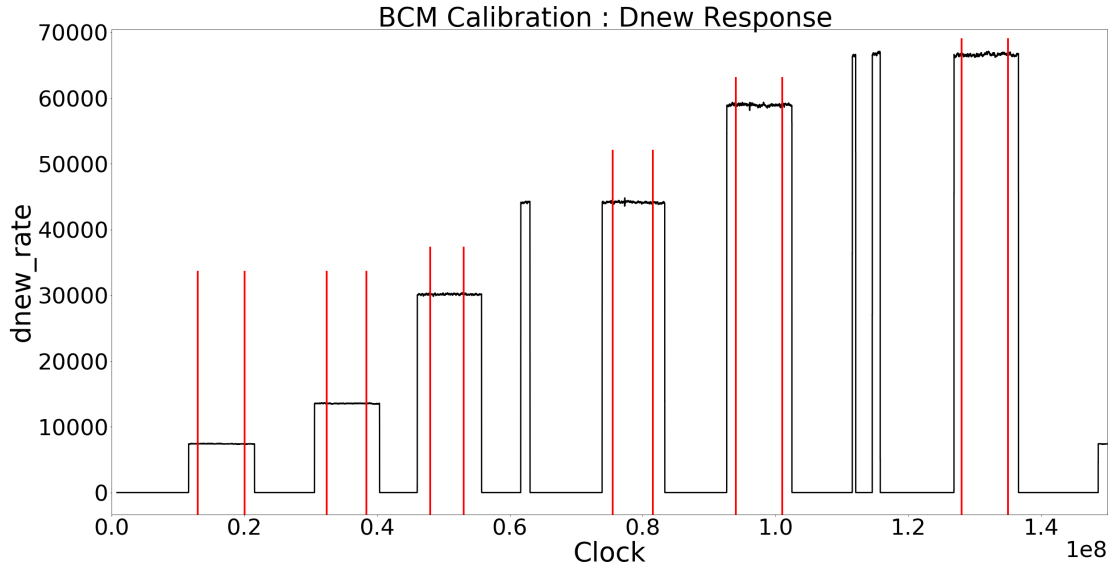


**Figure 2.10:** BCM calibration [28].

an amount of current in  $\mu\text{A}$ . In order to calibrate the BCMs in Hall A, a separate intrusive calibration of an unser must be done. The unser is calibrated by inserting a known current through a wire inside the beam pipe. The calibration of the unser is known to drift over time, which makes the unser unfeasible to use as the main source of charge calculation. Once the unser is calibrated, the BCM calibration procedure can be completed. The BCM calibration requires the delivery of the electron beam with unique procedure. This process consist of oscillating the beam on and off status while increasing the current. This process can be seen in figure 2.10. This stepping up procedure provides an adequate number of data points to complete a linear fit of the BCM frequency verses the calibrated unser current. The linear fit parameters supply a multiplicative gain and an additive offset for the calibration of the BCMs. Figure 2.11 shows a linear fit that provides gain and offset calibration constants for the BCM used in the calculation of charge.

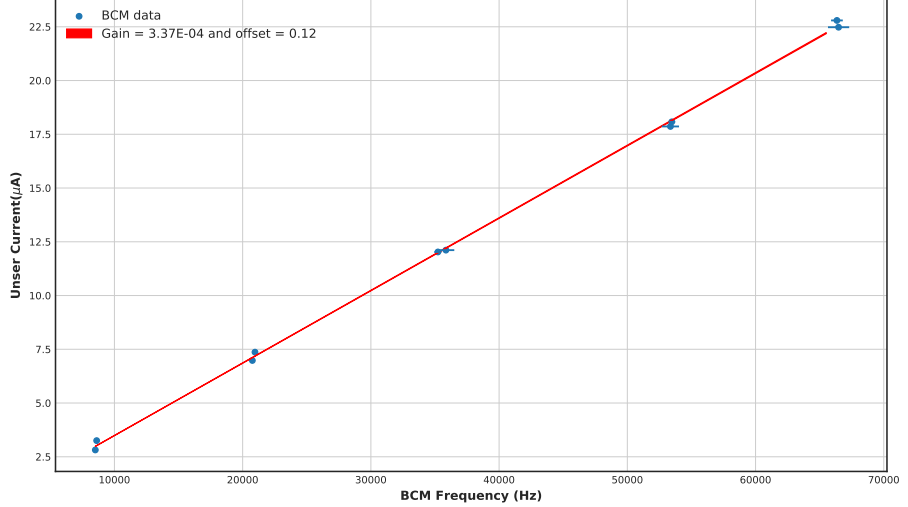
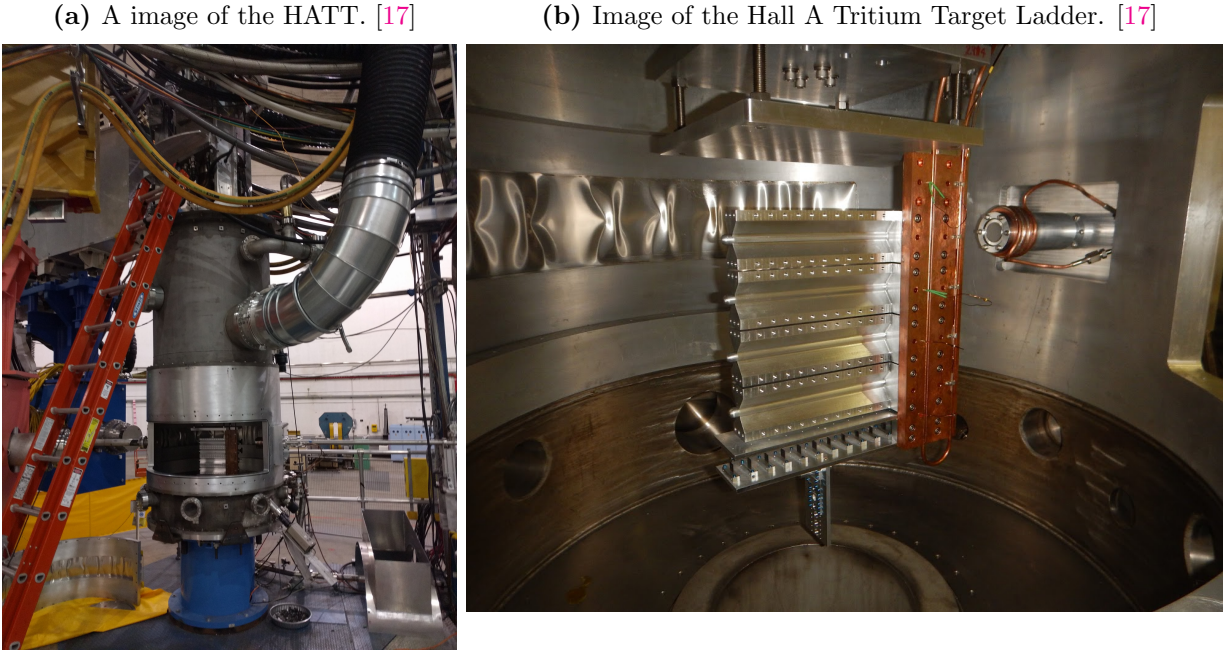


**Figure 2.11:** BCM frequency for BCM calibration [28].

## 2.3 Target

The Hall A Tritium Target(HATT) system was used for the Tritium run group of experiments. The HATT target chamber was repurposed from a previously used cryo-target chamber in order to reduce the financial cost of designing a new target chamber. The refurbishing of the cryo-target chamber consisted of adding in new safety features to prevent and mitigate a tritium leak. A 4 inch long collimator with an inner diameter of 0.4 inch was added inside of the target chamber but upstream of the target ladder to prevent the beam from striking the thin side wall of the aluminum cell. In case of a tritium leak in the target chamber, an exhaust system was installed to control the amount of tritium exposed to the Hall.[25] Figure 2.12 shows the HATT system with the target ladder in the home position and the scattering windows removed. A picture of the HATT ladder installed in the HATT system is shown if figure 2.12. The ladder contains both gaseous cells and solid targets. The MARATHON experiment had five gas cells. The top four of the gas cells were filled with tritium, deuterium, hydrogen, and  ${}^3\text{helium}$ , from top to bottom respectively. Due to safety restricts the tritium cell was not installed until the HATT system could be closed. The bottom most cell was left empty, to complete end cap subtractions. The lower half of the target

**Figure 2.12:** Target Images



ladder contains the solid targets used during the MARATHON experiment. Listed from top to bottom, the solid targets used were a pair of thick aluminum foils, carbon multifoil, single carbon foil, and a carbon foil with a 2mm diameter hole. The thick Al foils were used to aid the target window background subtraction. The multifoil target also known as the optics target was used to calibrate the z-axis reconstruction of the optics matrix. The single carbon foil and carbon hole were used to calibrate the BPMs and rasters and to determine the off set of the central line of the detector.

## 2.4 High Resolution Spectrometers

Electrons that successfully scatter from the target may end up in either of the two HRSs(High Resolution Spectrometers). The HRSs were designed to detect charged particles with a high degree of precision. In order to achieve a high level of resolution in momentum and angle, the HRSs were designed with a magnet configuration of  $QQD_nQ$  (quadrupole, quadrupole, dipole, and quadrupole). The vertical bending

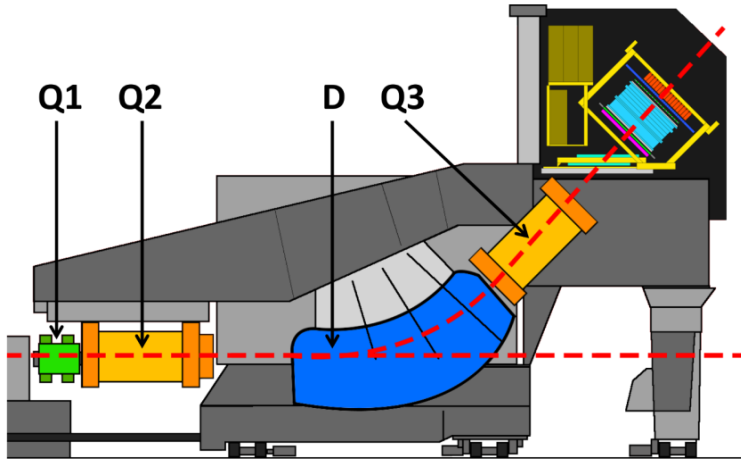


**Figure 2.13:** A side view of a HRS [1].

dipole provides the field required to transport the scattered particles through the  $45^\circ$  bending angle to the detector hut. A drawing of an HRS can be seen in figure 2.13. The first quadrupole(Q1) focuses the incoming electrons in the vertical plane. The following two quadrupoles (Q2 and Q3 provide transverse focusing. This optical design allows the use of extended gas targets with no substantial loss in solid angle[1]. The spectrometers were designed to perform various functions which include: triggering the data acquisition system (DAQ) when certain requirements are met, gathering the position and direction of individual particles to reconstruct a track, provide precise timing information for time of flight calculations, and identify many different particle types that pass through the detector system. In order for both the Left HRS (LHRS) and Right HRS (RHRS) to complete the required task, they contain a myriad of detectors. The HRSs use drift chambers, scintillators, cerenkov detectors, and shower calorimeters. Both the Left and Right HRSs contain two planes of scintillators to function has the main trigger for the detector package. The vertical drift chambers (VDC) that lay at the front of the detector in conjunction with the Shower that lies in the back of the detector provide information for reconstructing the particle tracks and precise timing. Particles are identified by the cerenkov, shower calorimeters, and pion rejectors that are contained in the left or right HRS. The

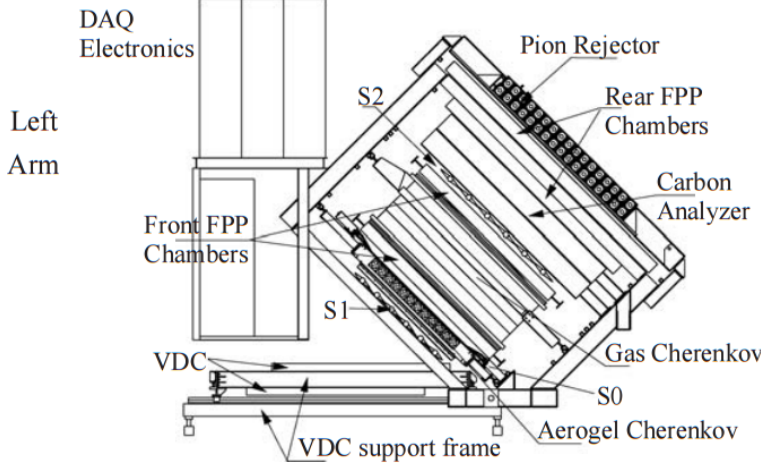


**Figure 2.14:** A view of both the left (top) and right (bottom) detector stacks inside the left and right HRS [1].

layout of the individual detectors that make up the left and right detector package are shown in figure 2.14 [1].

#### 2.4.1 Vertical Drift Chambers

Each of the spectrometers housed in Hall A contains two vertical drift chambers(VDC). Each VDC incorporates two planes of crossing sense wires. Shown in figure 2.15, the two planes of the VDC lie a distance of 0.335m apart [10]. The lower plane of the VDC is positioned at the approximate focal plane of the HRS and lies in the horizontal plane of the Hall A coordinate system. The sense wires located in the VDCs cross orthogonally. They are offset by  $45^\circ$  in respect to the dispersive and non-dispersive directions. Each plane of the VDC uses 368 sense wires, with 4.24 mm between each wire. The signals from these wires are transmitted to the electronics via a set of printed circuit boards that contain a 16-channel connector and twisted pair ribbon cables. These ribbon cables transmit the VDC signal to a set of common stop TDC with 0.5 ns resolution [10]. The VDC sense wires are held at ground potential between two planes of high-voltage. Particles that enter the gas filled VDC, collide with molecules of an argon(62%) and ethane (38%) mixture [1]. This collision causes the ionization of the gaseous mixture producing drift electrons.

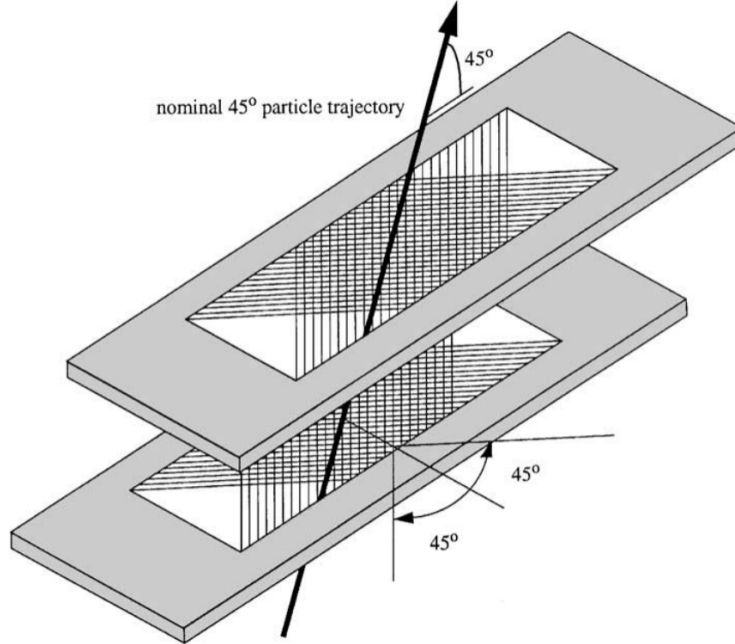


**Figure 2.15:** A sketch of the two VDC planes in the HRSs with a particle traveling through the detector at  $45^\circ$ .[10].

Particles that transverse the VDCs will travel through regions close to several sense wires. As the incident particle ionizes gas in each of these regions, the VDC sense wires pick up the corresponding signal from the drift electrons. The drift electrons will travel to the sense wires via the parallel electron field lines until the electrons get close to the sense wires. Once close to the sense wires, the electron field transitions to a radial field and the drift electrons then move to the sense wires. An example of a drift electron's trajectory is shown in figure 2.16, in which a cluster of 5 wires sense scattered particle.

The drift chamber's performance is constantly monitored throughout the experiment. The efficiency of an individual wire is determined by an algorithm that scans a plane for an event that fires a cluster of wires. A wire is determined to be efficient for that event if it fired along with its two nearest neighbors. This efficiency calculation is used during the online analysis to keep track of the performance of the VDCs and to assist in the maintenance of the HRSs throughout the experiment.

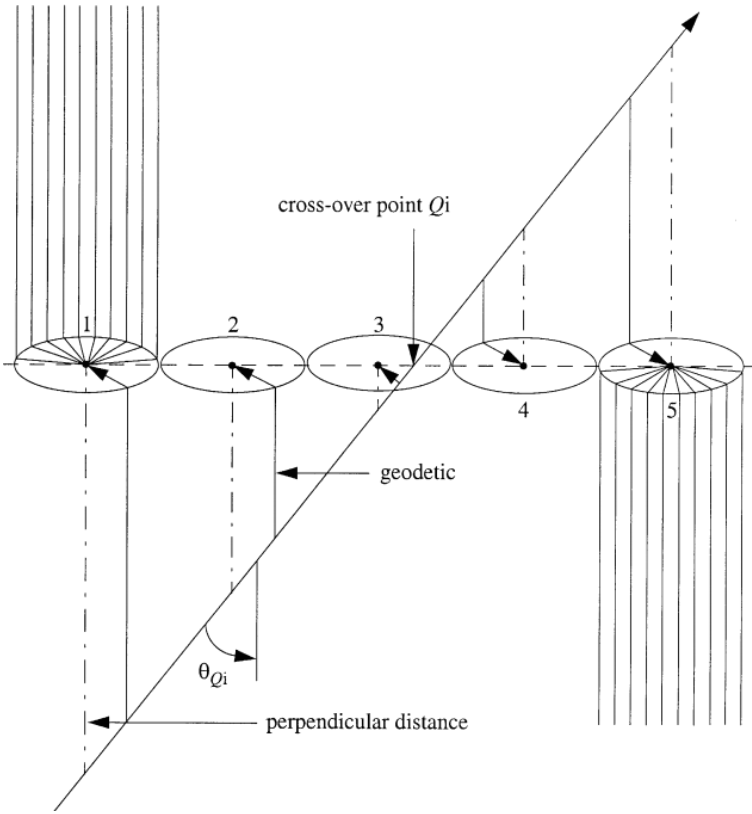


**Figure 2.16:** A possible track that causes signals in wires. The drift electrons will follow the arrow path. The dot/dashed lines correspond to the projected distance used to reconstruct the path of the incident particle. The transition point from parallel to radial field lines is represented by the ellipses. [10]

The VDC's main task during an electron counting experiment is to determine the track of the scattered electron. The track of the electron is used to ascertain the electron's scattering momentum and scattering angle. Due to the electron's relativistic nature the primary ionization event for each wire region happens simultaneously compared to the resolution of the TDCs. The common stop TDCs used for the VDC signals record the amount of time from drift electron's signal in the sense wires to the stop signal formed by the trigger. This creates a high TDC signal for short drift distances. The raw TDC values recorded by the VDC include time associated with the signal but also the time required to form the trigger and time of flight for electrons between the VDCs and detectors used in the formation of a trigger. The calibration of the VDC removes these extra sources of time in the TDC

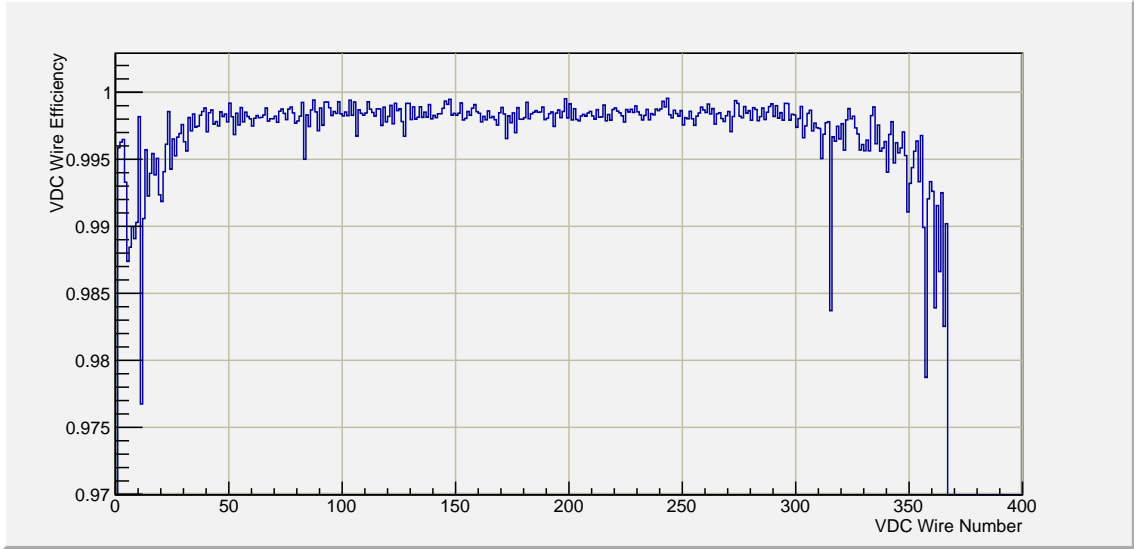


**Figure 2.17:** The VDC efficiency for one plane of wires.

signal. In order to calibrate the VDC raw signals, a reference time is determined for every wire on every plane. This references time ( $t_0$ ) is chosen as the TDC value of the sharp decrease on the outside of the peak in region C shown in figure 2.18. The time recorded from the TDCs is used to construct a location of the ionization event for each sense wire across the trajectory of the scattered electron. The analyzing software will use these drift distance from the four VDC planes to find a track for the scattered electron.

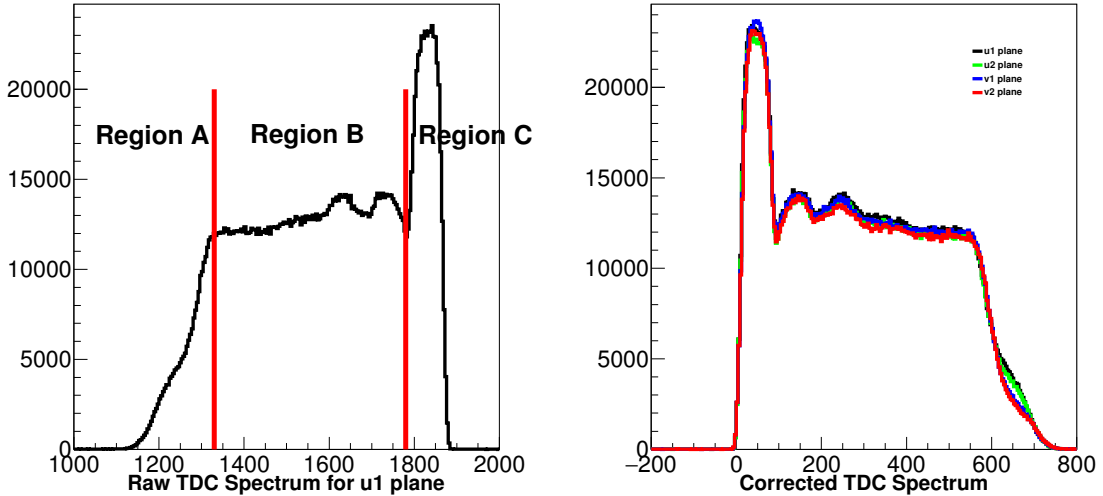


**Figure 2.18:** Histograms of VDC signals before(left) and after(right) calibration of  $t_0$ [19].

- Region A: In this region, the point of primary ionization is far from the sense wire. As this distance increases, the chance of detecting the transversing particles by this wire is decreased.
- Region B: The probability of sense wires detecting a primary ionization event in this region are uniform due to the uniform electric field though out the region.
- Region C: The primary ionization position for these events are very near the sense wire and the electric field from this area is going to change to radial shape and the probability to detect a particle is going to increase in this area. The sense wire exist in the region, so the ionization event will have a minimum distance. This is shown in the sharp decline on the outside of the peak in region C. [19]

## 2.4.2 Scintillators

A pair of scintillator planes form the primary triggering apparatus for the HRSs. The planes of scintillator S0 and S2 consist of a collection of plastic scintillating paddles with photo multiplier tubes(PMTs) attached to both ends of the paddle. S0 the first scintillator in the stack consist of one scintillating paddle in a vertical direction. S2, the second scintillator was build with 16 overlapping paddles with PMTs attached to both ends. As electrons enter the scintillating plastics energy is absorbed by the material scintillating light. This light is detected by the PMTs on either side of the bar. The passing of the electron can happen at positions at an unequal distances from the PMTs on a scintillator bar. These relative differences cause a distortion in the timing calculation in the TOF known as the time walk effect. The scintillators are used in the calculation of  $\beta$ , the  $v$  to  $c$  ratio. Beta is calculated using the time of flight(TOF) between the two scintillator planes and distance traveled between the points of interaction. Once calibrated, each plane has a time resolution

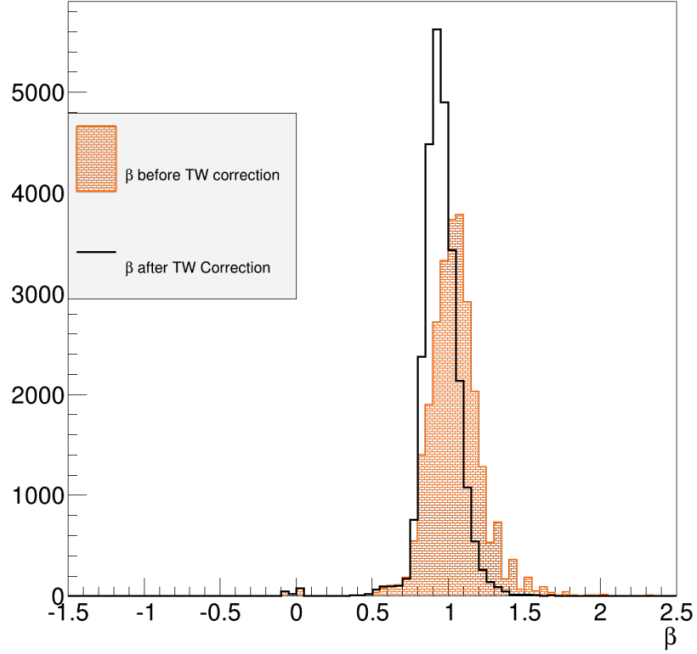


**Figure 2.19:** Histogram of  $\beta$  before and after time walk correction.

of about 0.3 ns. This high time resolution and quick response makes the scintillators the perfect detector to form the main trigger.

### 2.4.3 Cherenkov

After a particle passes through S0, it will enter the large gas chamber for the gas cherenkov(GC). The GC is filled with  $CO_2$  with an index of refraction of 1.00041. This high index of refraction creates a momentum threshold of 0.017 GeV/C for electrons, 4.8 GeV/C for pions, and 32 GeV/c for protons[4]. Relativistic particles entering the GC will produce a cone of cherenkov radiation. This cone of light will be focused by a set of mirrors on the back plane of the GC. These mirrors direct the focused light onto a set of PMTs. An depiction of the GC from a top down perspective is shown in figure 2.20. The raw data recorded from the GC is in the

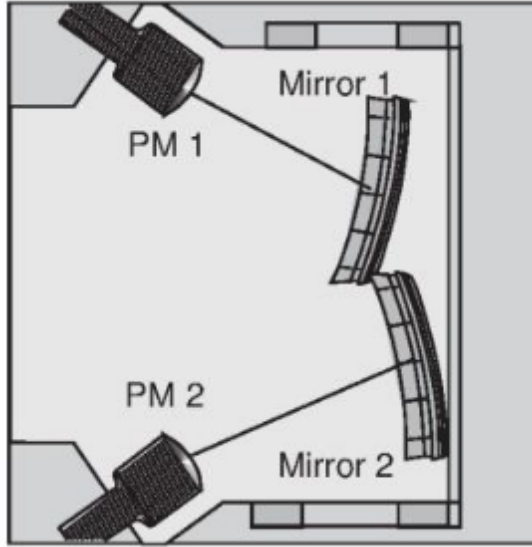


**Figure 2.20:** Top down depiction inside the GC [4].

form of raw ADC, or the size of the pulse seen by the PMT. In order to use this information, the ADC input needs to be calibrated. For the GC, two parts of the signal needs to be calibrated. Each ADC channel sees a different amount of noise and signal background from electronic fluctuations. This signal background is defined as

the ADC pedestal, and is the first calibration offset determined. Figure 2.21 shows the raw signal from one cherenkov PMT. This signal shows the pedestal at approximately 5800 ADC channels. The pedestal is subtracted from the raw ADC signal to normalize the background electronic noise for all PMT-ADC pairs in the cherenkov. The second calibration for the GC ADC signals is the photo electron peak. The voltage used to power the PMTs in the cherenkov is tuned before the experiment to allow the PMT to give the best pedestal to signal ratio while also preserving the life of the PMT and signal quality. This forces a different signal strength to be seen by each PMT for the same amount of light experienced in the chamber. The photo electric peak in the ADC signal is then normalized to the same value across all PMTs by a gain factor.

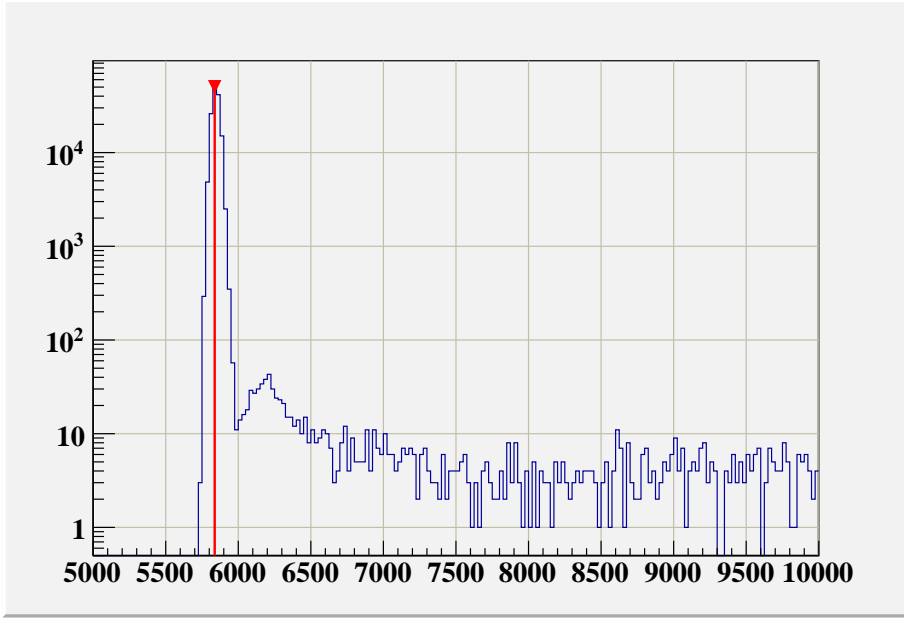


**Figure 2.21:** The raw signal captured from a single cherenkov PMT, PMT[1], with a fit to the pedestal peak and a line draw to demonstrate its ADC channel number.

The GC's main task during an experiment is to help in the identification of particles(PID). During the MARATHON experiment, the GC was used to differentiate between negatively charged pions and electrons that passed through the detector. MARATHON used the GC in PID for data capture and analysis.

During data capture, the GC signal was used in the formation of the main trigger. Using the GC in the trigger by forcing a certain threshold in signal strength from the GC, allowed for the exclusion of many unwanted events. During the analysis of MARATHON data, pion suppression was done using the GC signal and signals from the calorimeter.

#### 2.4.4 Calorimeter

The last detector in the spectrometer that particles interact with is the lead glass calorimeter. The Left HRS (LHRS) calorimeter system is made up of the preshower(PS) and shower(SH). The PS contains two columns of 24 blocks of lead glass with a PMT attached to the end. The SH has five columns, and each column has 16 blocks with a PMT. The right HRS'(RHS) calorimeter system is constructed of the pion rejector 1(PR1) and the pion rejector 2(PR2). The two PRs on the RHS consist of 34 blocks arranged in two, 17 block columns.

The calorimeters are used during the analysis process to help in PID. As high energy electrons pass through the dense leaded glass, the electron will lose its energy through bremsstrahlung radiation resulting in the emission of a photon. These photons begin a electromagnetic shower through the creation of positron-electron pairs. The shower of photons are detected by the PMTs attached to each block. The amount of energy contained in the scattered electron is directly proportional to the amount of photons generated during the shower.

The signal from the calorimeters is recorded as an ADC. These ADC signals need to be calibrated similar to the cherenkov detector, subtracting the pedestal and determining the normalizing gain factor to match all PMT-ADC combinations. The total signal seen from the calorimeter can be seen in figure 2.22a. In order to use this ADC signal to help ID particles, the calorimeter needs an energy calibration. The calibration process uses a  $\chi^2$  minimization. Equation 2.5 demonstrates the

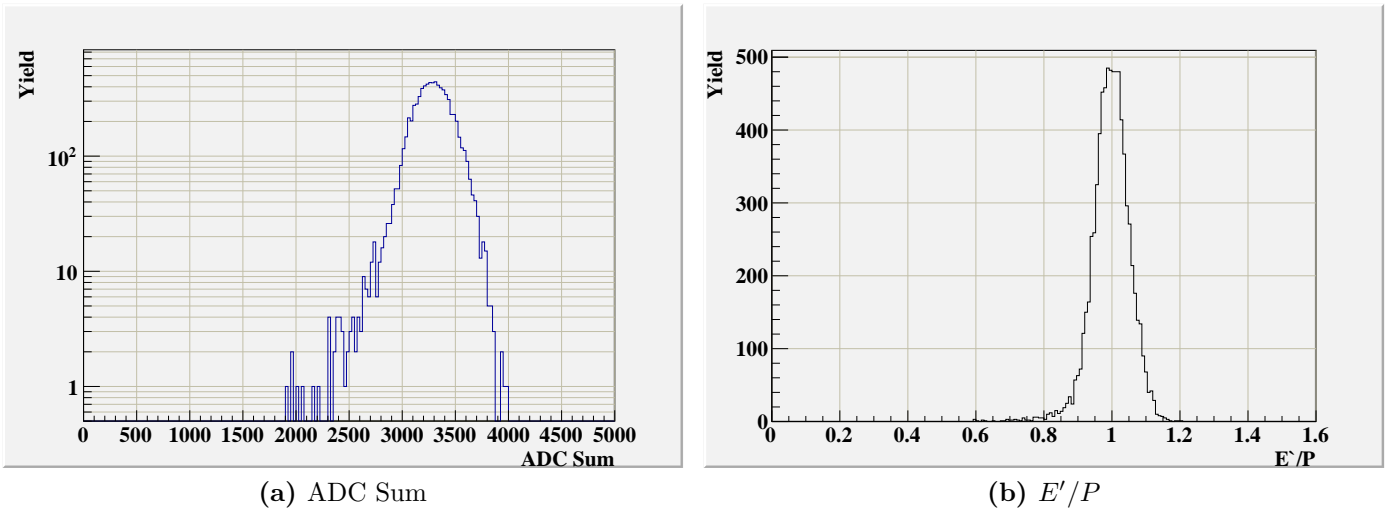


**Figure 2.22:** Left: The sum of all ADC channels from the LHRS calorimeters. Right: The total energy deposited into the LHRS calorimeter scaled by the momentum setting. Electron cuts have been applied.

minimization technique applied. In this equation,  $C_j$  is the calibration coefficient being determined for the calorimeter block  $j$ .  $Cal_{ij}^{ADC}$  is the ADC signal received from block  $j$  during event  $i$ , and  $p_i$  is the momentum of the electron being detected.

$$\frac{\partial \chi^2}{\partial C_i} = \sum_i^{Events} \left( \sum_j^{Blocks} C_j * Cal_{ij}^{ADC} - p_i \right)^2 = 0 \quad (2.5)$$

Using these calibration constants, the ADC signal in figure 2.22a can be turned in the calibrated data in the histogram show in figure 2.22b. This can be used to from PID selection cuts, removing any unwanted background events.

## 2.5 Trigger Setup

## 2.6 Kinematic Settings

LHRS

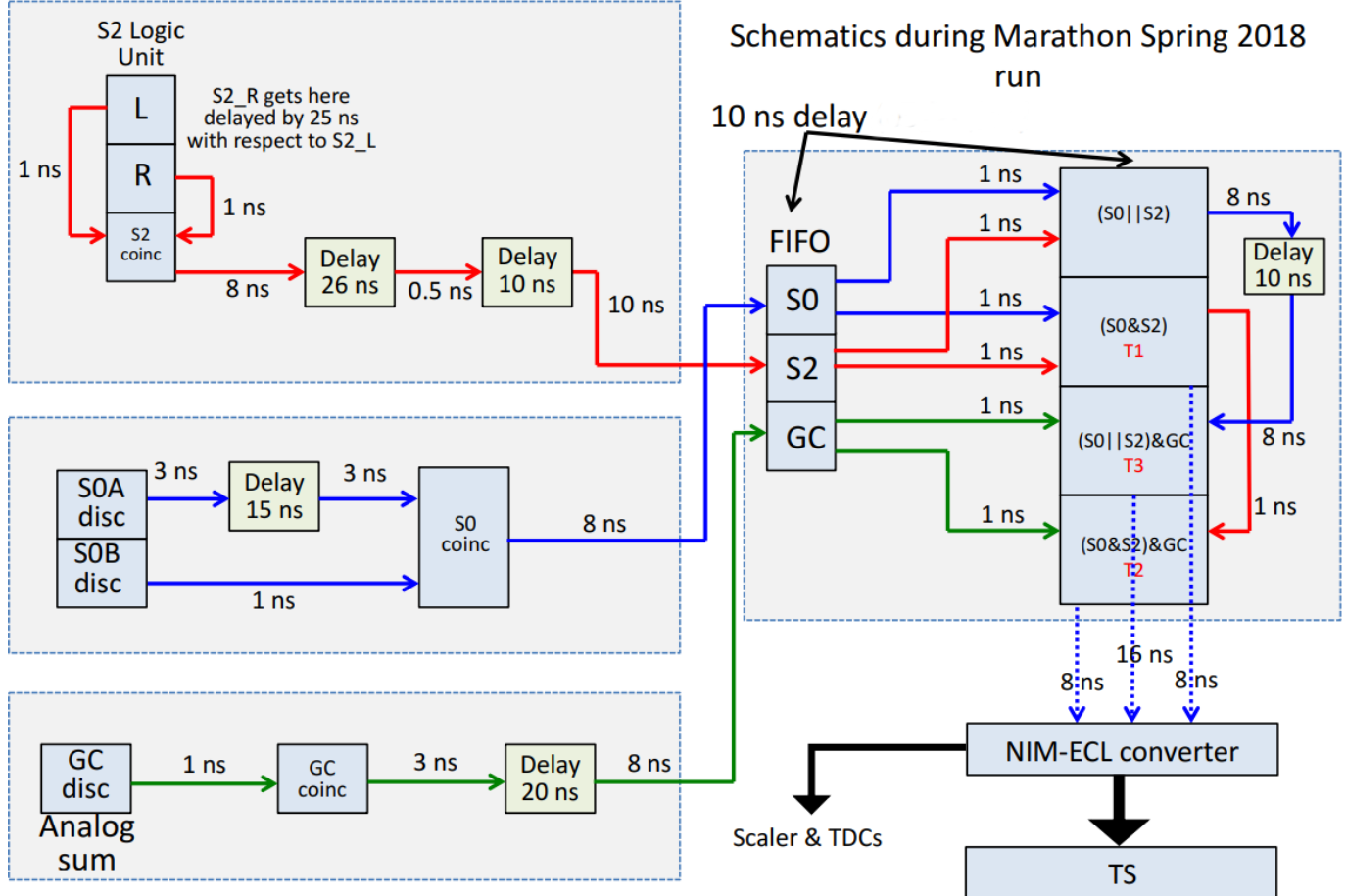


**Figure 2.23:** Scematic drawing of the trigger logic and timing for the MARATHON experiment [15].

# Chapter 3

## Data Analysis

### 3.1 Efficiencies

The high resolution spectrometers are capable of detecting a myriad of particles that track through the detectors. The design of an experimental trigger uses the properties of the individual detectors to capture data of meaningful events. Many accidentals, background, and unwanted events trigger the data acquisition system, and some good electrons are missed by our DAQ. The removal of these unwanted events takes place during analysis via software cuts. Restricting the applicable signal from certain detectors through different cuts allows for the rejection of background particles and prevents contamination in the yield extraction.

#### 3.1.1 Computer and electronic Lifetime

The signal from events that fire the DAQ travel through electronics like amplifiers and logic modules on its way to be recorded by the TDCs and ADCs. The processing of these signals require time at each stage. During that time another event will be discarded due to limitations in the hardware. This time when the DAQ system cannot handle another event is known as the dead-time of the system. Lifetime therefor is the percentage of time when an event can be recorded. The lost events need to be account

### Livetime for each kinematic

Kin	1	2	3	4	5	7	9	11	13	15
LiveTime	0.947	0.969	0.981	0.986	0.992	0.996	0.997	0.998	0.998	0.998

**Table 3.1:** Livetime during the MARATHON experiment calculated using trigger 2.

for during the analysis process. The lifetime of the DAQ system for the MARATHON experiment was measured by determining the percentage of events that were recorded relative to the number of events that fired the corresponding trigger. The lifetime for the MARATHON experiment depended on the rate of events. The lifetime during the highest rate kinematic was determined to be 0.947, and climbs to 0.998 for the highest angle setting. Listed in table 3.1 are the calculated values for lifetime at each kinematic.

### 3.1.2 Particle Identification Efficiency

One of the largest sources of contamination for the MARATHON experiment are negatively charged pions. These pions are removed through software cuts made in the total signal from the ten cherenkov PMTs(photomultiplier tubes) and the energy deposited into the blocks of both layers of the calorimeter. Electrons can be identified by their behavior in the spectrometer. High-quality electrons will track through the entire detector stack to deposit most of their energy into the total calorimeter system and creating a large amount of light in the cherenkov. Though this knowledge tight cuts can be used to study the efficiency of the particle identification system. Plotting the signal in the cherenkov versus the energy deposited into both layers of the calorimeter allows for visual representation of the sampling cuts made in the efficiency studies, which can be seen in figure 3.1.

$$GE_{sample} = \text{Known electron sample from tight cut}$$

$$GE_{pass} = GE_{sample} \text{ and pass identification cut} \quad (3.1)$$

$$Electron_{eff} = \frac{GE_{pass}}{GE_{sample}}$$

### Cherenkov sum versus Total Energy deposited

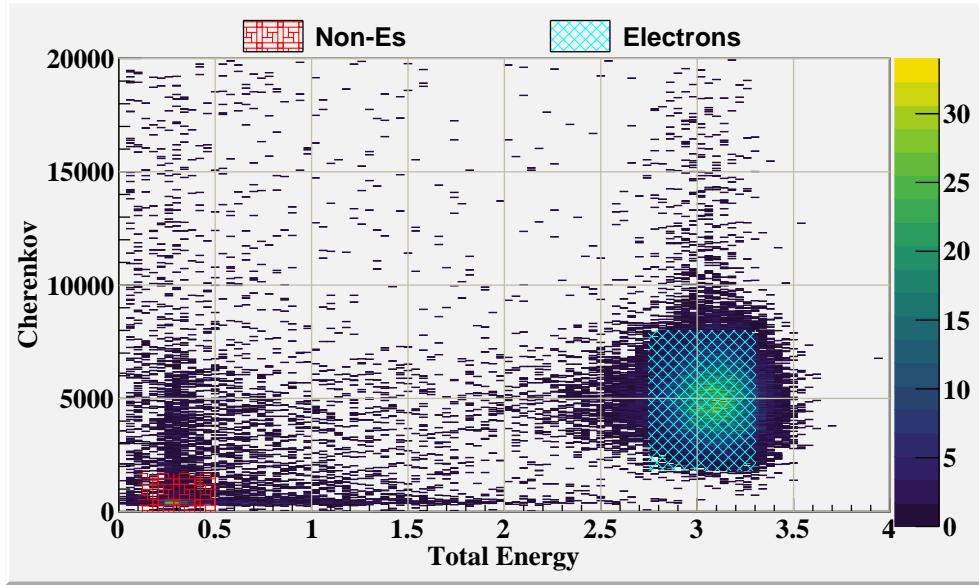


**Figure 3.1:** Two dimensional plot of the cherenkov sum versus Total Energy deposited, including electron sampling in teal and non-electron sampling in red.

The efficiencies of the spectrometer's particle identification(PID) detectors were determined by using the first calorimeter layer, the second calorimeter layer, and the cherenkov to provide samples of good electrons and other particles. The PID efficiency of the individual detectors was determined using equation 3.1. The good electron sample for calculating the efficiency of the single detector was defined by sampling through the other two detectors. Sampling through the two layers of the calorimeter is shown in figure 3.2a for the first layer of the calorimeter and 3.2b for the second layer. The cherenkov good electron sample is shown in figure 3.2c. The electron sample from the cherenkov is contaminated by delta particles and a combination of unknown particles. These unidentified background particles are known to be relativistic due to the amount of light seen in the cherenkov. However, the events do not deposit enough energy into the calorimeter system to be considered as a good electron that scatter from our target through the detector. Using sampling in one layer of the calorimeter

## Particle ID and efficiency sampling for PID detectors

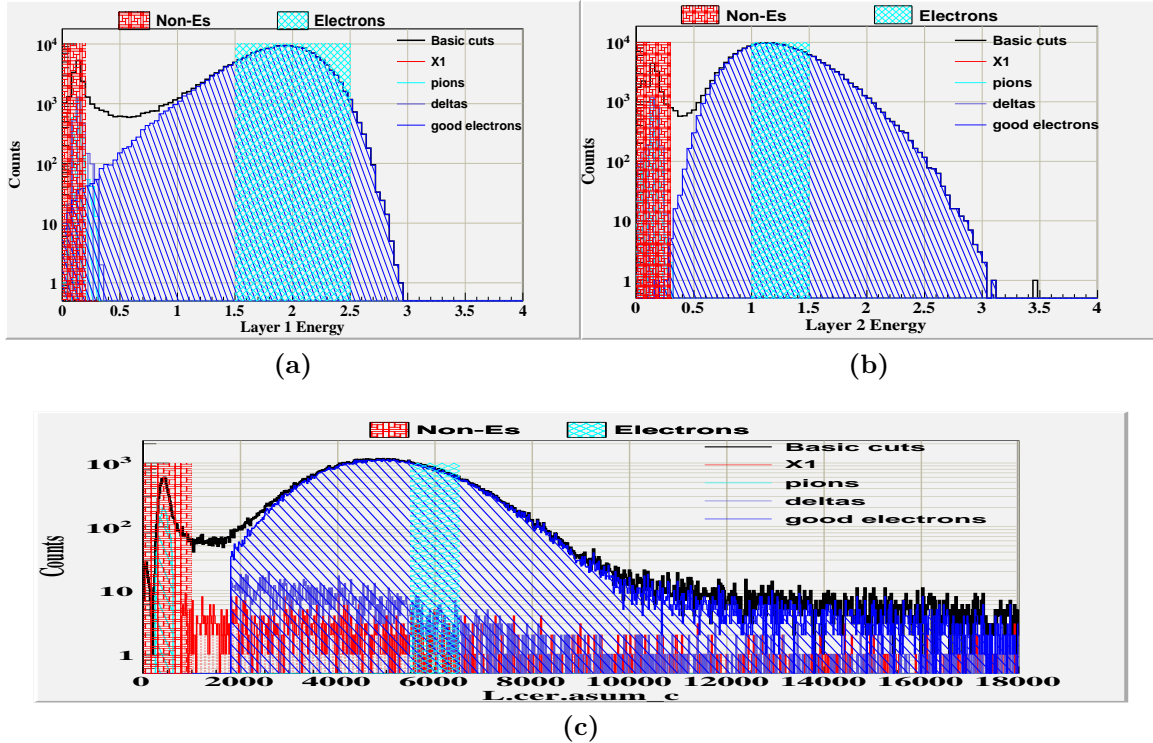


**Figure 3.2:** Electrons and other back ground particles identified via cuts in the total calorimeter and the gas cherenkov shown in the individual layers of the calorimeters and the cherenkov. Sampling cuts for Electrons in teal and Non-Electrons in red.

and the cherenkov, these unwanted low energy particles are rejected from sampling for efficiency calculations. The electron selection PID efficiency for the three PID detectors was determined at each kinematic setting to be approximately 98% . The efficiency was determined to be independent of the kinematic setting. Only small fluctuations were seen during the study, these small changes are due to decrease in statics, and all of the results fall within statical uncertainty of being independent of kinematic setting. The non-electron suppression efficiency was determined as part of this PID efficiency study to ascertain how many back ground particles leak into our sample of good electrons after cuts our made. The suppression efficiency of the cherenkov suffered due to the contamination of the relativistic low energy particles. Combining the two calorimeter detectors with the cherenkov increased the overall

PID efficiency for each detector for all kinematics.

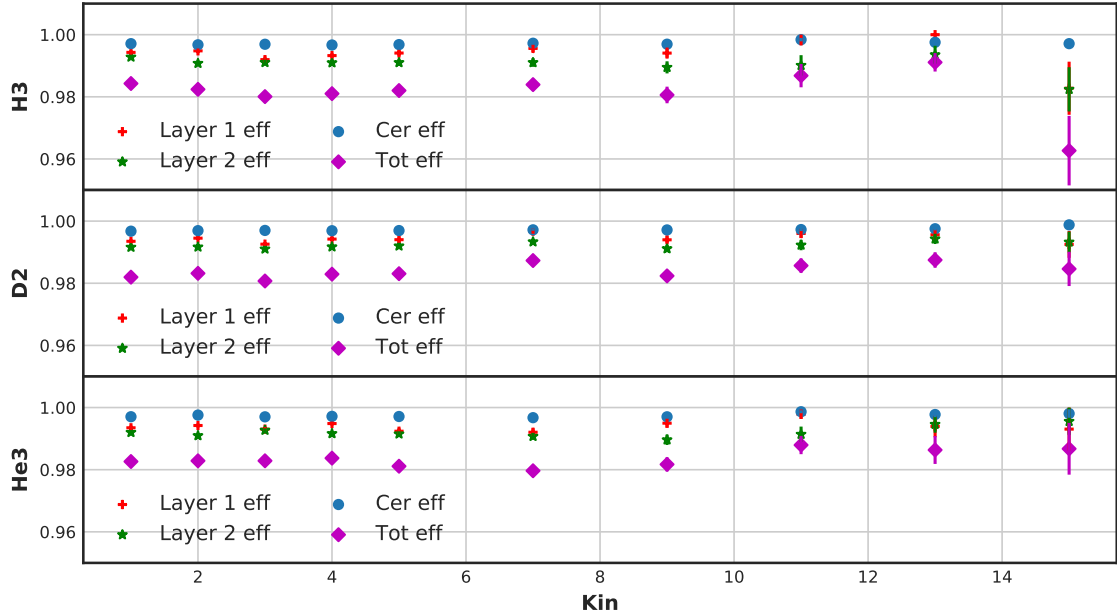


**Figure 3.3:** The PID efficiency for the cherenkov and both layers of the calorimeter, including the overall total PID efficiency for each of the gas targets at all of the kinematics.

suppression efficiency for the spectrometer to 99.9% over the entire kinematic range of the MARATHON experiment.

### 3.1.3 Trigger Efficiency

The process of capturing data from the two HRSs begins with the firing of a trigger. The trigger design for MARATHON focused on triggering for electrons and reducing the amount of other particles. Figure ?? describes the design of MARATHON's main trigger and efficiency triggers. MARATHON's main trigger, trigger 2, consist of a  $(S_o \& S_2) \& Cer$ . Due to inefficiencies of the electronics, logic, and detectors an event can produce a false trigger or a high quality electron may not fire the main trigger.

A low threshold in the cherenkov allows for an inclusive trigger limiting the overall number of quality electrons missed, but allows for a large quantity of false

## Trigger efficiency for the MARATHON experiment

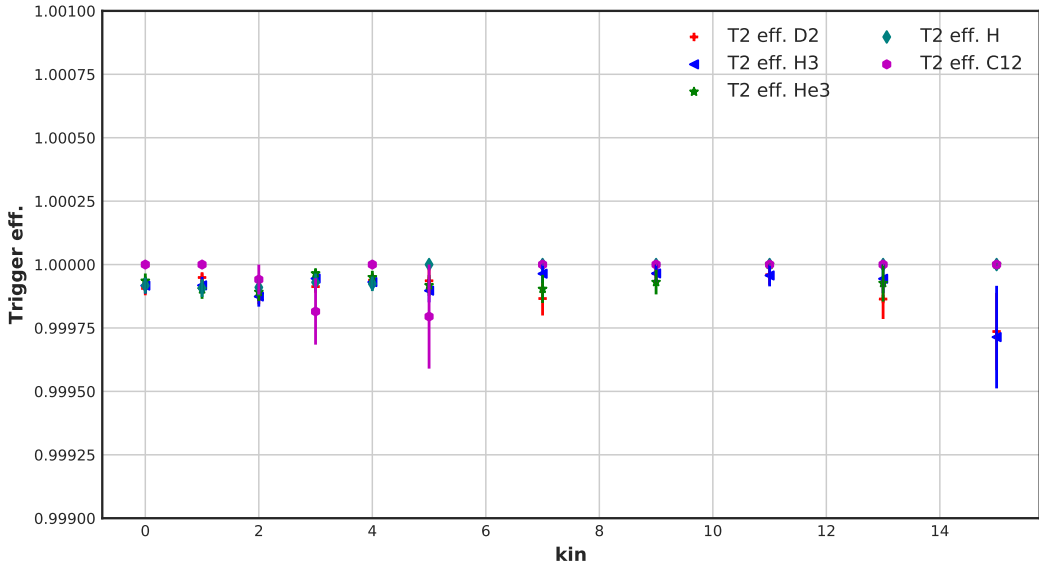


**Figure 3.4:** Trigger efficiency of trigger 2 for different targets at all kinematics calculated via sampling from trigger 1.

triggers. Software PID cuts prevent the contamination of false positives from trigger inefficiencies. The tight PID software cuts removes the false positive inefficiency from the trigger design and is then considered in the PID efficiencies. The trigger inefficiency caused by missed high quality electrons was then calculated by sampling the high quality electrons in trigger 1, ( $S_o \& S_2$ ). This ties the efficiency of trigger 2 with the performance of the scintillators. The efficiency of the two scintillating planes in conjunction is calculated by using sampling in trigger 3, ( $S_o | S_2 \& Cer$ ) with strict PID cuts in both layers of the calorimeters and requiring a hit in the cherenkov. The two scintillator planes in conjunction have an efficiency greater than 99.7% for all kinematics. Combining the trigger efficiency of the main trigger shown in figure 3.4 with the performance of the scintillators give an over all efficiency for the trigger of the MARATHON experiment of greater than 99.6%.

## Tracking efficiency for the MARATHON experiment

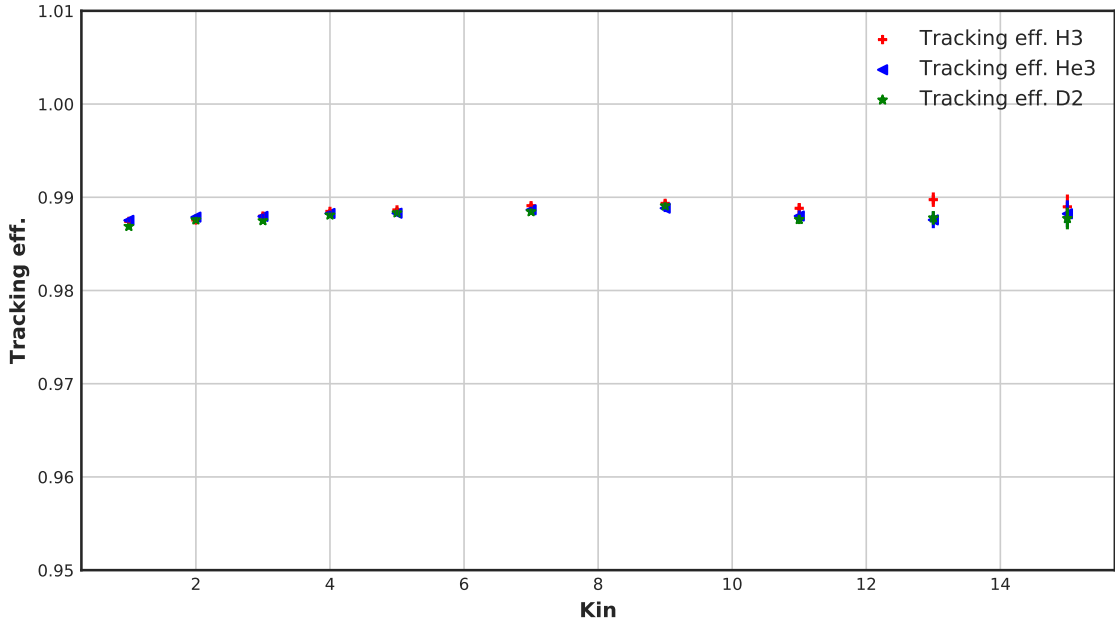


**Figure 3.5:** Tracking efficiency of the VDCs for different targets at all kinematics.

### 3.1.4 Tracking Efficiency

Particles that travel through our detector could originate from sources wanted or unwanted. In order to control the source of the scatter electrons, we use a particle's track to identify its source. The signals received via the VDC is used to produce a particles track from the target to end of the spectrometer. The largest source of inefficiency for the VDCs are incorrectly identified tracks. High quality electrons that transverse the spectrometer should only have one good track, calculated via the tracking package in the analysis software. The capability of the VDCs to determine a good electron event's one good track is known as the one track efficiency for the VDCs. Quantitatively the one track efficiency ( $\epsilon_{VDC}$ ) can be obtained via:

$$\epsilon_{VDC} \equiv \frac{N_{1track}}{N_{all}} \quad (3.2)$$

Where the number of good electron events that have one good track is defined as  $N_{1track}$ , and  $N_{all}$  are all of the electrons rather they have a good track or not. The

good electron selection is made via PID cuts in the calorimeter and cherenkov, and cuts in the ADC and TDC of the scintillators. Direct cuts in the signal of the scintillators were made to include the nominal acceptance cuts, which were produced through tracking software. The tracking efficiency of HRSs during the MARATHON experiment is shown in figure 3.5 for the three gas targets during all kinematic ranges. The efficiency of the VDCs is not relative to the angle of the spectrometer. So the uniform tracking efficiency across all kinematics is expected and helps eliminate any concerns of the performance of the VDCs during the experiment.

## 3.2 Background Subtraction

The purpose of this analysis is to study the DIS cross sections of deuterium, helium-3, and tritium. The sample of scattered events used to determine the cross section of a given nuclear target then needs to be cleaned of any contamination produced from other targets and processes. The electrons detected by the spectrometers can be electrons that scatter from our chosen target, scattered from a source other than our target, or produced through process other than DIS scattering. The two sources of contamination for the MARATHON experiment are events scattered from the aluminum end caps of the target cell and pair produced electrons via photon interaction.

### 3.2.1 End Caps

The target cells used during the MARATHON experiment are shown in figure 2.12. The majority of the events from the end caps can be removed easily via a cut in the reconstructed quantity of reaction vertex along the beam axis. The relatively large density thickness of the aluminum end caps cause a large amount of end cap contamination. The majority of the electrons that scatter from the end caps can be removed through software cuts in the reaction vertex along the beam axis(z). Show

### Scattering vertex along the beam axis.

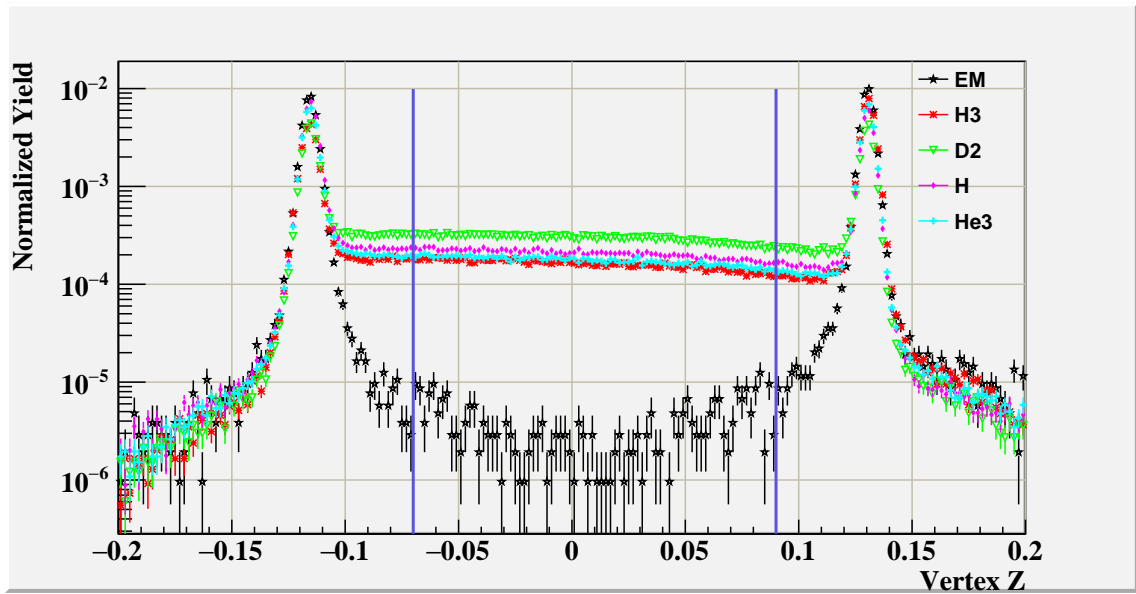


**Figure 3.6:** Comparison of the scattering vertex along the z axis for the empty target(EM) and the gas targets at kin. 4.

in figure 3.6 is a comparison of the reaction vertex of the electron events between the gaseous targets and the empty cell target at kinematic 4. The yield is normalized by the number of event in the histogram to remove any bias from the amount of time of beam on target. The empty target results in figure 3.6, demonstrate the form of scattering off of the aluminum windows of our target cell. Using the reconstructed vertex location of the scattering origin, the vast majority of the events from the windows can be removed. This vertex cut is shown by the two vertical blue lines. Only events that lie within these two line are considered good electrons from our chosen target.

The empty cell vertex z disruption does have content within the vertex cut. These events that remain after the cut are corrected for via an end cap contamination factor. This factor is calculated by determining the ratio of the number of good electrons that scatter from the empty cell and from each gas cells, resulting in ratio of  $(\frac{Yield_{EC}}{(Yield_{Gas}+Yield_{EC})})$ . Where the subscript EC denotes events from the end caps.

The correction factor applied to the yield calculation is defined as:

$$ECC = 1 - \left( \frac{Yield_{EC}}{(Yield_{Gas} + Yield_{EC})} \right) \equiv \frac{Yield_{gas}}{(Yield_{Gas} + Yield_{EC})}$$

### 3.2.2 Pair Produced Electrons

The high energy scattering interaction used to create deep inelastic scattering events can produce high energy photons and pions. The high energy photons that have energy greater than 1.022 MeV can convert into  $e^+e^-$  pairs when the photons interact with a medium. A correction for the number of back ground electrons produced via a pair production process was calculated by determining the amount of positrons produced from equal targets and kinematics. The yield of positrons were measured for kinematics one through five. The results were used to construct a function to determine the amount of contamination at high  $x_{Bj}$  kinematics. Figure 3.7 shows the amount of positron contamination for tritium and an exponential fit to extrapolate over the entire ranged in  $x_{Bj}$  for the MARATHON experiment.

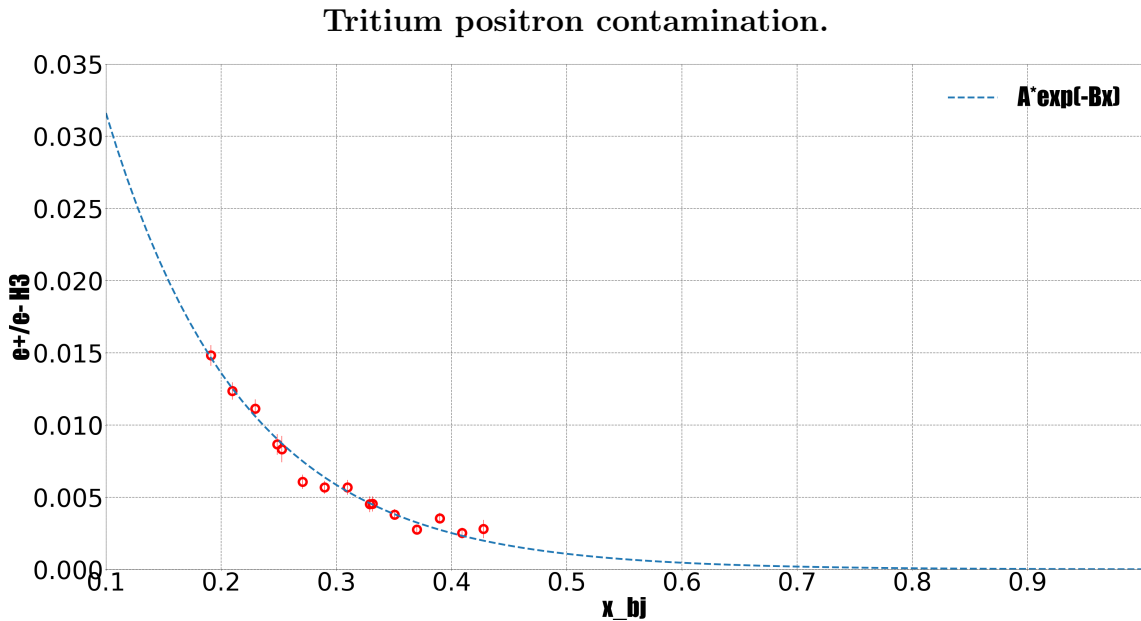


**Figure 3.7:** The ratio of positron events to electrons for tritium [33].

# **Chapter 4**

## **Results**

# Chapter 5

## EMC Simulation

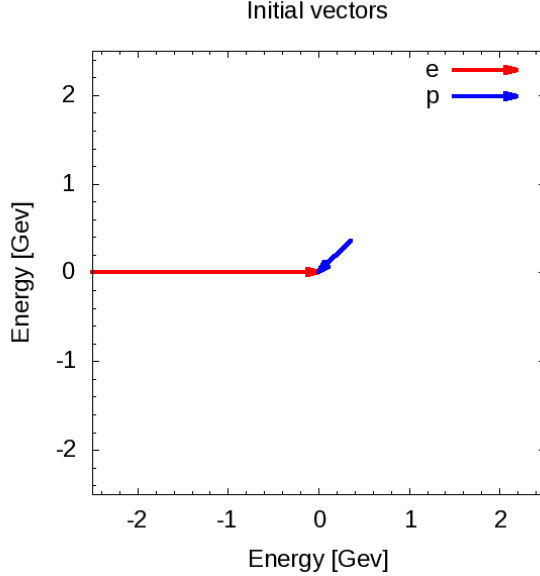
Nuclei are systems of nucleons that interact strongly. The characteristic scale for the nucleons momentum is approximately the Fermi momentum,  $k_F \approx 200 - 270 \text{ MeV}/c$  [13]. However because of the strongly repulsive nature of the nucleon-nucleon interaction at short distances prevents two nucleons from laying in close proximately to each other. This strong interaction demands the presence of high-momentum components in the nuclear ground state wave function. A simulation was designed to phenomenologically study the effect of these high-momentum components on the nuclear EMC effect. This program was designed in two phases. The first phase used simple elastic scattering and a single value for the targets momentum to investigate overall effect of different target momentum on the yield in bins of  $x_B$ . The second phase of the simulation was created to lay out the effect of using different momentum distributions on the yield for the EMC effect region of  $x_B$ , 0.3 to 0.7.

### 5.1 Investigation

This simulation phenomenologically investigates the effect of a moving target on the EMC effect by scattering a beam of electrons off of a moving proton. The target protons are comprised of a directional vector of  $0^\circ$  to  $360^\circ$  in respect to the incoming electron beam and a momentum between 0 and 1 GeV/c. Figure 5.1 contains a

possible event for the simulation. The electron approaches with 2.5 GeV of energy and collides with a proton moving with a momentum of 0.5 GeV/c with an angle of 45° in respect to the electron trajectory.

**Figure 5.1:** Example of the electron beam(red) with a energy of 2.5 GeV and the proton(blue) with angle of 45° in respect to the electron and with a momentum of 0.5 GeV/c.



Using conservation of momentum and conservation of energy in elastic collisions, this simulation calculates the final state of the electron and proton after the scattering event by randomly selecting a scattered direction for the electron. The vector representation of the scattered products are shown in figure 5.3a. In order to make these calculations systematic and to study cross sections models the simulation transform each event into the rest frame of the target before scattering.

## 5.2 Transformation

The Simulation completes a set of Lorentz invariant rotations and boost for each event to transform the lab frame of the electron and proton collision into the rest frame of the proton. First the simulation takes the initial proton and electron vectors

and rotates them to align the proton vector to the horizontal axis, shown in figure 5.2b. This rotation uses the angle between the proton and the electron defined as  $\lambda$ . This allows for a straight forward calculations for the Lorentz factors  $\beta$  and  $\gamma$  and to boost into the rest frame of the target proton, figure 5.2c. Once in the boosted frame, the angle between the electron and the horizontal axis is defined as  $\delta$ . Right before the simulation starts to calculate the scattered products, it completes one more rotation to align the electron vector with the horizontal axis, figure 5.2d, to make the scattering calculation systematic and unconditional.

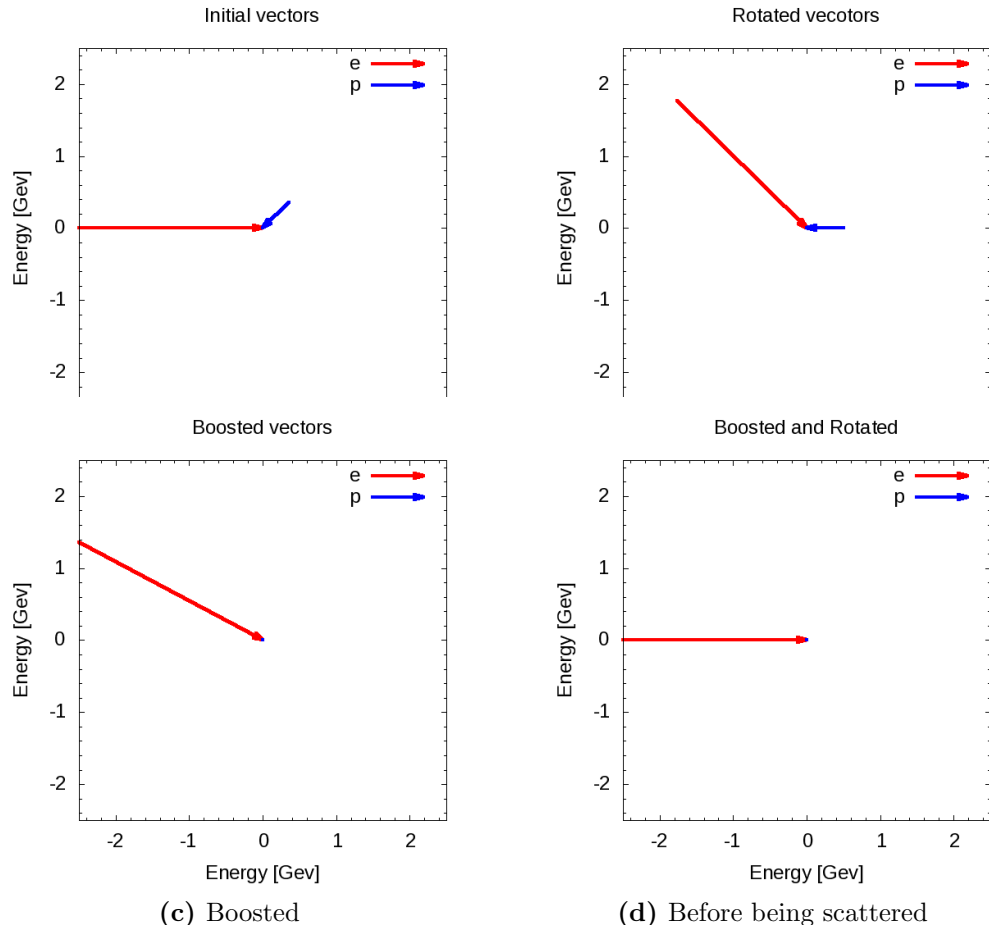


**Figure 5.2:** Vector representations of the momentum for the incoming electron(red) and target proton(blue) with units of GeV for each phase of their transformations before scattering.

In order to gain a more complete understanding of the scattering products, the program completes a set of transformations to move from the rest frame of the target proton to the beginning lab frame. After the simulation calculates the scattered products it begins to transform back by beginning with a rotation by the angle  $\delta$ , figure 5.3b. Followed by the inverse of the previously used Lorentz boost. The last transformation, a rotation by  $\lambda$ , transforms the frame back into the lab frame. A proton vector and electron vector in the lab frame are the final products of the simulation. An image of the electron and proton vectors for each transformation can be found in figure 5.3. These vectors allow for calculation of kinematic variables such as Bjorken  $x$  and the four-momentum transfer ( $Q^2$ ). This simulation will complete these steps for many electron and proton combinations.

### 5.3 Results

This electron scattering simulation produced results for two stages. The firsts stage used a fix proton momentum for each run to compare the yield in bins of  $x_B$ . Figure 5.4 shows the results for three different runs, each having a unique fixed proton momentum. The red histogram represents a run with a proton momentum of 0 Gev/c. The result is an elastic peak at  $x_B$  of one. The blue histogram contains the results having a fixed proton momentum of 0.25 GeV/c. Increasing the initial momentum of the proton spreads the events into two peaks. The scattering interactions that form the peak above 1  $x_B$  are produced by events were the proton's initial directional vector are orientated towards the electron. The events that produce an  $x_B$  below 1 have a proton direction pointing away from the electron initially. Doubling the proton's initial momentum from 0.25 GeV to 0.50 GeV causes these peaks two spread out furtherer in  $x_B$ .

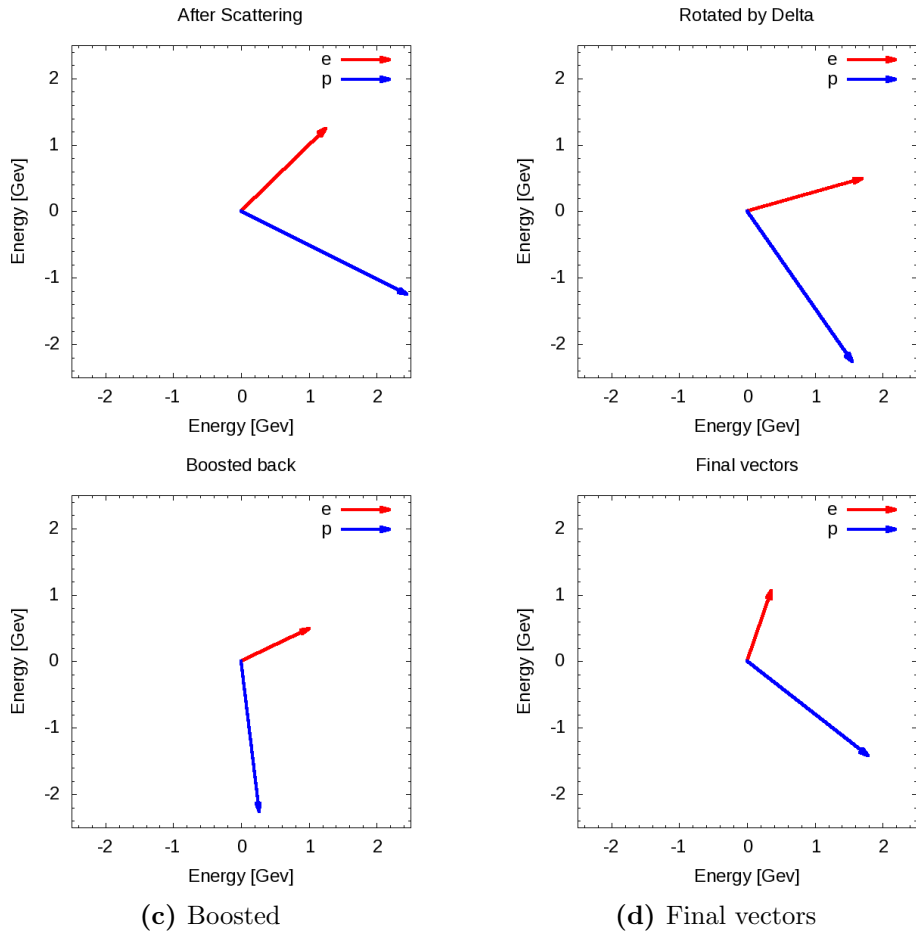
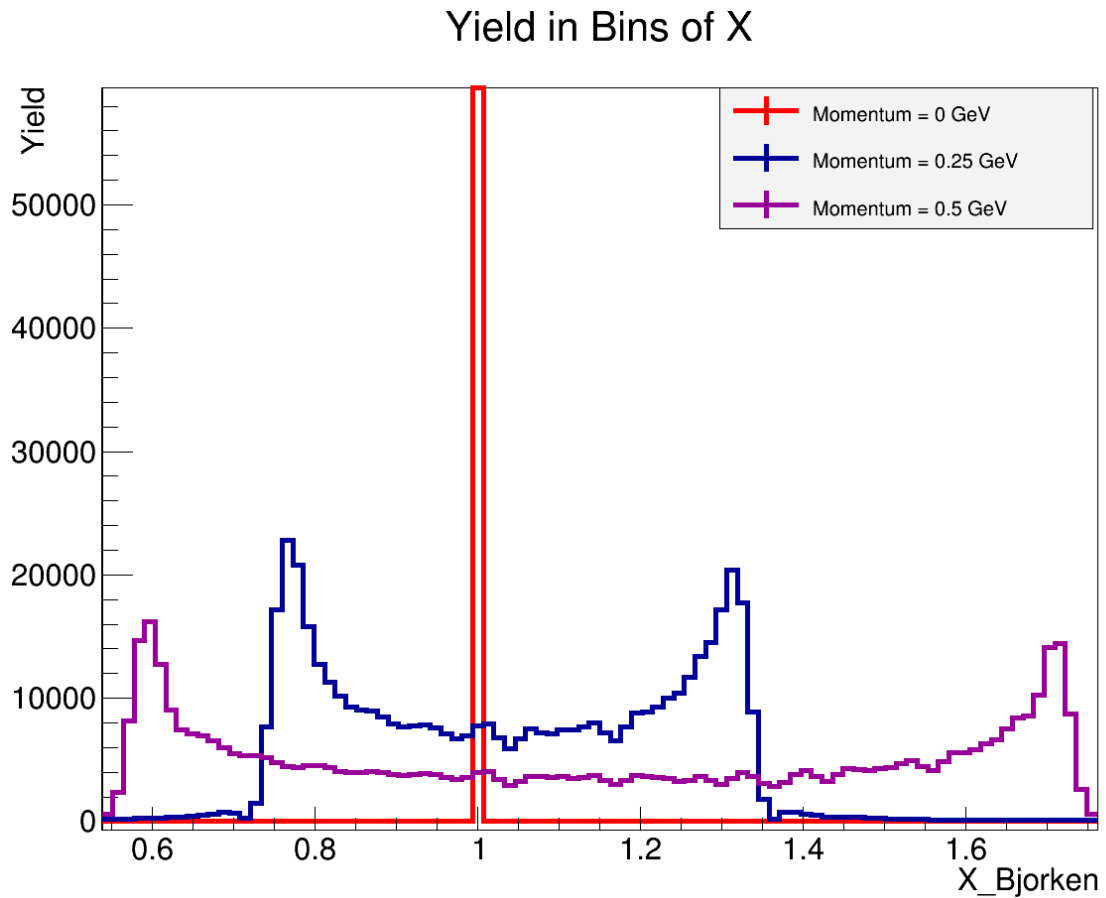


**Figure 5.3:** Vector representations of the momentum for the incoming electron(red) and target proton(blue) with units of GeV for each phase of their transformations after scattering).

**Figure 5.4:** Simulation results for fixed momentum protons. Three runs with unique proton momentum.



# Chapter 6

## Conclusion

# Bibliography

# Bibliography

- [1] J. Alcorn et al. Basic Instrumentation for Hall A at Jefferson Lab. *Nucl. Instrum. Meth.*, A522:294–346, 2004. [vi](#), [vii](#), [14](#), [16](#), [17](#), [27](#), [28](#)
- [2] K Nakamura and. Review of particle physics. *Journal of Physics G: Nuclear and Particle Physics*, 37(7A):075021, jul 2010. [vi](#), [7](#)
- [3] John Arrington, Aji Daniel, Donal Day, Nadia Fomin, Dave Gaskell, and Patricia Solvignon. A detailed study of the nuclear dependence of the EMC effect and short-range correlations. *Phys. Rev.*, C86:065204, 2012. [10](#)
- [4] T. Averett, B. Zhao, and B Wojtekhowski. Bigbite heavy gas cherenkov detector at 6.6 and 8.8 gev. [vii](#), [34](#)
- [5] M. Breidenbach, J. I. Friedman, H. W. Kendall, E. D. Bloom, D. H. Coward, H. DeStaebler, J. Drees, L. W. Mo, and R. E. Taylor. Observed behavior of highly inelastic electron-proton scattering. *Phys. Rev. Lett.*, 23:935–939, Oct 1969. [8](#)
- [6] Gennady M. Briskin. *Diffractive Dissociation in ep Deep Inelastic Scattering*. PhD thesis, Tel Aviv U., 1998. [6](#)
- [7] A. Daniel, J. Arrington, and D. Gaskell. Measurements of the EMC effect in few-body nuclei at large x. *AIP Conf. Proc.*, 1369:98–105, 2011. [11](#)
- [8] J. Denard and J. Sahar. High accuracy beam current monitor system for cebaf’s hall a. Chicago, 2001. Particle Accelerator Conference. [vi](#), [23](#)

- [9] J. Edelmann, G. Piller, Norbert Kaiser, and W. Weise. Resonances and higher twist in polarized lepton nucleon scattering. *Nucl. Phys.*, A665:125–136, 2000. [10](#)
- [10] K.G. Fissum et al. Vertical drift chambers for the hall a high-resolution spectrometers at jefferson lab. *Nuclear Instruments and Methods in Physics Research Section A: Accelerators, Spectrometers, Detectors and Associated Equipment*, 474(2):108 – 131, 2001. [vii](#), [28](#), [29](#), [30](#)
- [11] David J. Flay. *Measurements of the Neutron Longitudinal Spin Asymmetry A1n and Flavor Decomposition in the Valence Quark Region*. PhD thesis, Temple University, Philadelphia, PA, Aug 2014. [vi](#), [2](#), [3](#), [22](#), [23](#)
- [12] D.F. Geesaman, K Saito, and A Thomas. The nuclear emc effect. *Annual Review of Nuclear and Particle Science*, 45(1):337–390, 1995. [10](#)
- [13] J. Gomez, R. G. Arnold, P. E. Bosted, C. C. Chang, A. T. Katramatou, G. G. Petratos, A. A. Rahbar, S. E. Rock, A. F. Sill, Z. M. Szalata, A. Bodek, N. Giokaris, D. J. Sherden, B. A. Mecking, and R. M. Lombard-Nelsen. Measurement of the  $a$  dependence of deep-inelastic electron scattering. *Phys. Rev. D*, 49:4348–4372, May 1994. [10](#), [50](#)
- [14] Tyler Hague. Calibrating the hall a raster. Technical report, JLab, 2019. [vi](#), [21](#), [22](#)
- [15] Florian Hauenstein and Reynier Cruz Torres. Tritium trigger setup. [vii](#), [38](#)
- [16] D. Higinbotham. The emc effect still puzzles after 30 years - cern courier. <http://cerncourier.com/cws/article/cern/53091>, April 2013. (Visited on 01/04/2016). [vi](#), [2](#), [9](#), [11](#)
- [17] Doug Higinbotham. Target images, December 2017. [26](#)

- [18] R Hofstadter. Nuclear and nucleon scattering of high-energy electrons. *Annual Review of Nuclear Science*, 7(1):231–316, 1957. [4](#)
- [19] Tyler Kutz Hanjie Liu Mike Nycz Tong Su Jason Bane, Tyler Hague and Evan McClellan. Marathon pass 2 analysis primer. [vii](#), [32](#)
- [20] R. Kazimi et al. Four Beam Generation for Simultaneous Four-Hall Operation at CEBAF. In *Proc. of International Particle Accelerator Conference (IPAC'16), Busan, Korea, May 8-13, 2016*, number 7 in International Particle Accelerator Conference, pages 4240–4242, Geneva, Switzerland, June 2016. JACoW. doi:10.18429/JACoW-IPAC2016-THPOY060. [14](#)
- [21] Henry W. Kendall. Deep inelastic scattering: Experiments on the proton and the observation of scaling. *Rev. Mod. Phys.*, 63:597–614, Jul 1991. [6](#), [8](#)
- [22] Christoph W. Leemann, David R. Douglas, and Geoffrey A. Krafft. The continuous electron beam accelerator facility: Cebaf at the jefferson laboratory. *Annual Review of Nuclear and Particle Science*, 51(1):413–450, 2001. [14](#), [15](#)
- [23] Simona Malace, David Gaskell, Douglas W. Higinbotham, and Ian Cloet. The Challenge of the EMC Effect: existing data and future directions. *Int. J. Mod. Phys.*, E23:1430013, 2014. [8](#)
- [24] R. W. McAllister and R. Hofstadter. Elastic scattering of 188-mev electrons from the proton and the alpha particle. *Phys. Rev.*, 102:851–856, May 1956. [2](#)
- [25] David Meekings. Hall a tritium target, 2017. [25](#)
- [26] Jonathan Mulholland. *SANE’s Measurement of the Proton’s Virtual Photon Spin Asymmetry,  $A_1^p$ , at Large Bjorken  $x$* . PhD thesis, Virginia U., 2012. [vi](#), [8](#), [14](#)
- [27] P R Norton. The emc effect. *Reports on Progress in Physics*, 66(8):1253, 2003. [vi](#), [10](#)

- [28] Mike Nyzc. *EMC effect in Tritium*. PhD thesis. vi, 24, 25
- [29] G. Palacios-Serrano, F. Hannon, C. Hernandez-Garcia, M. Poelker, and H. Baumgart. Electrostatic design and conditioning of a triple point junction shield for a 200 kv dc high voltage photogun. *Review of Scientific Instruments*, 89(10):104703, 2018. 14
- [30] B. Povh. *Particles and nuclei: an introduction to the physical concepts*. Springer, 1999. 1, 2, 4, 5, 6, 7
- [31] Tom Powers, Lawrence Doolittle, Rok Ursic, and Jeffrey Wagner. Design, commissioning and operational results of wide dynamic range bpm switched electrode electronics. *AIP Conference Proceedings*, 390(1):257–265, 1997. 18
- [32] J. Seely et al. New measurements of the european muon collaboration effect in very light nuclei. *Phys. Rev. Lett.*, 103:202301, Nov 2009. 2, 10, 11
- [33] Tong Su. Positron correction analysis. viii, 48
- [34] Richard E. Taylor. Deep inelastic scattering: The early years. *Rev. Mod. Phys.*, 63:573–595, Jul 1991. 8
- [35] Hall A Tech. Ep method. [http://hallaweb.jlab.org/equipment/beam/energy/ep\\_web.html](http://hallaweb.jlab.org/equipment/beam/energy/ep_web.html). (Accessed on 06/28/2016). 23
- [36] L.W. Whitlow, E.M. Riordan, S. Dasu, S. Rock, and A. Bodek. Precise measurements of the proton and deuteron structure functions from a global analysis of the slac deep inelastic electron scattering cross sections. *Physics Letters B*, 282(3):475 – 482, 1992. 8
- [37] Pengjia Zhu et al. Beam Position Reconstruction for the g2p Experiment in Hall A at Jefferson Lab. *Nucl. Instrum. Meth.*, A808:1–10, 2016. vi, 18, 19

# Appendix